



Comparing calculated microphysical properties of tropical convective clouds at cloud base with measurements during the ACRIDICON-CHUVA campaign

5 *Ramon Campos Braga¹, Daniel Rosenfeld², Ralf Weigel³, Tina Jurkat⁴, Meinrat O. Andreae^{5,9}, Manfred Wendisch⁶, Mira L. Pöhlker⁵, Thomas Klimach⁵, Ulrich Pöschl⁵, Christopher Pöhlker⁵, Christiane Voigt^{3,4}, Christoph Mahnke³, Stephan Borrmann³, Rachel I. Albrecht⁷, Sergej Molleker⁸, Daniel A. Vila¹, Luiz A. T. Machado¹, and Paulo Artaxo¹⁰*

10 ¹Centro de Previsão de Tempo e Estudos Climáticos, Instituto Nacional de Pesquisas Espaciais, Cachoeira Paulista, Brasil

²Institute of Earth Sciences, The Hebrew University of Jerusalem, Israel

³Institut für Physik der Atmosphäre, Johannes Gutenberg-Universität, Mainz, Germany

⁴Institut für Physik der Atmosphäre, Deutsches Zentrum für Luft- und Raumfahrt (DLR),

15 Oberpfaffenhofen, Germany

⁵Multiphase Chemistry and Biogeochemistry Departments, Max Planck Institute for Chemistry, 55020 Mainz, Germany.

⁶Leipziger Institut für Meteorologie (LIM), Universität Leipzig, Stephanstr. 3, 04103 Leipzig, Deutschland

⁷Instituto de Astronomia, Geofísica e Ciências Atmosféricas, Universidade de São Paulo, São Paulo, Brazil

20 ⁸Max Planck Institute for Chemistry (MPI), Particle Chemistry Department, Mainz, Germany

⁹Scripps Institution of Oceanography, University of California San Diego, La Jolla, California 92037, USA

¹⁰Instituto de Física (IF), Universidade de São Paulo (USP), São Paulo, Brazil

Correspondence to: Ramon C. Braga (ramonbraga87@gmail.com)

Abstract: Reliable aircraft measurements of cloud microphysical properties are essential for understanding liquid
25 convective cloud formation. In September 2014, the properties of convective clouds were measured with a Cloud
Combination Probe (CCP), a Cloud and Aerosol Spectrometer (CAS-DPOL), and a cloud condensation nuclei
(CCN) counter on board the HALO (High Altitude and Long Range Research Aircraft) aircraft during the
ACRIDICON-CHUVA campaign over the Amazon region. An intercomparison of the cloud drop size distributions
(DSDs) and the cloud water content derived from the different instruments generally shows good agreement within
30 the instrumental uncertainties. The objective of this study is to validate several parameterizations for liquid cloud
formation in tropical convection. To this end the directly measured cloud drop concentrations (N_d) near cloud base
were compared with inferred values based on the measured cloud base updraft velocity (W_b) and cloud condensation
nuclei (CCN) vs. supersaturation (S) spectra. The measurements of N_d at cloud base were also compared with drop



concentrations (N_d) derived on the basis of an adiabatic assumption and obtained from the vertical evolution of cloud
 35 drop effective radius (r_e) above cloud base. The results demonstrate agreement of the measured and theoretically
 expected values of N_d based on CCN, S , W_b at cloud base, and the height profile of r_e . The measurements of $N_{CCN}(S)$
 and W_b did reproduce the observed N_d . Furthermore, the vertical evolution of r_e with height reproduced the observa-
 tion-based nearly adiabatic cloud base drop concentrations, N_d . Achieving such good agreement is possible only with
 40 accurate measurements of DSDs. This agreement supports the validity of the applied parameterizations for continen-
 tal convective cloud evolution, which now can be used more confidently in simulations and satellite retrievals.

1. Introduction

The understanding of cloud formation and its influence on the global hydrological cycle and radiation budget is
 45 fundamental for improving weather and climate forecasting models (Ten Hoeve et al., 2011; Jiang and Feingold,
 2006; Kohler, 1999; Rosenfeld et al., 2008; Stephens, 1984). Cloud microphysical models pursue to reproduce
 atmospheric processes based on physical relationships developed from field experiments and remote sensing
 observations in different parts of the globe (Silva Dias et al. 2002; Machado et al. 2014; Fan et al. 2014; Rosenfeld
 et al. 2014b). Data from aircraft probes provide opportunities to validate and improve cloud models.

50 An assessment of the validity of data from cloud probes is essential before the results can be implemented into cloud
 models. According to previous studies, the number concentration of cloud droplets (N_d) expected at cloud base
 mainly depends on atmospheric conditions just below cloud base, i.e., updraft wind speed and the supersaturation
 (S) activation spectra of cloud condensation nuclei [$N_{CCN}(S)$] (Pinsky et al., 2012; Reutter et al., 2009; Twomey,
 1959). From cloud condensation nuclei counter (CCNC) measurements across a range of supersaturations (S), the
 55 parameters N_0 and k are estimated from Twomey's formula (Twomey, 1959):

$$N_{CCN} = N_0 \cdot S^k \quad (1)$$

where N_0 is the cloud condensation nuclei (CCN) concentration at $S=1\%$ in cm^{-3} , and k is the slope parameter
 (Twomey, 1959). Equation 1 is an analytical representation of the observational data within the measured range of S ,
 which in our case represents the observed CCN spectrum from 0.2 to 0.55 %. Note, however, that Eq. 1 does not
 60 allow a reliable extrapolation of $N_{CCN}(S)$ beyond this range (Pöhlker et al., 2016).

The parameters N_0 and k are estimated from data measured below cloud base along with updrafts wind speed
 measurements at cloud base (W_b). The values of W_b , N_0 , and k are used for calculating the theoretical cloud droplet
 concentration from Eq. 2 (Twomey, 1959) below:

$$N_{dT} = 0.88 \cdot N_0^{\frac{2}{k+2}} \cdot (0.07 \cdot W_b^{1.5})^{\frac{k}{k+2}} \quad (2)$$

where N_{dT} are the estimated cloud base drop concentrations in cm^{-3} . Here we compare the measured N_d to N_{dT} by
 65 substituting in Eq. 2 the measured $N_{CCN}(S)$ in the form of N_0 and k , along with the measured W_b .

Equations 1 and 2 are a rather simplistic parameterization. More advanced methods, using the hygroscopicity
 parameter κ (kappa) are more accurate to represent the CCN spectrum (Pöhlker et al., 2016). However, in this study,



using Twomey's parameterization is advantageous, because the CCN measurements were performed within the range of 0.2-0.55 %, where the estimation of the N_0 and k parameters using Eq. 1 does not incur significant errors in comparison with more advanced methods (Pöhlker et al., 2016). Furthermore, Twomey's parameterization also allows calculating the effects of updraft wind speed on N_{dr} as a function of N_0 and k .

Another approach to estimate the number concentration of CCN that are expected to nucleate as droplets at cloud base is through the use of the k -Köhler model (Petters and Kreidenweis, 2007). Based on a given dry aerosol particle size distribution (ASD), the k -Köhler model with prescribed W_b simulates the expansion and cooling of air as well as the resulting changes in relative humidity and the related hygroscopic growth of aerosol particles and further condensational growth of cloud droplets. The input to this approach depends strongly on the measured ASD and κ (Reutter et al., 2009).

Measurements of ASD by a Passive Cavity Aerosol Spectrometer Probe (PCASP) and Ultra-High-Sensitivity Aerosol Spectrometer (UHSAS) probes were available during the ACRIDICON (Aerosol, Cloud, Precipitation, and Radiation Interactions and Dynamics of Convective Cloud Systems) - CHUVA (Cloud processes of the main precipitation systems in Brazil: A contribution to cloud resolving modeling and to the GPM [Global Precipitation Measurements]) campaign (Wendisch et al., 2016). However, calculating κ from the combined CCN, PCASP, and UHSAS measurements below cloud resulted in unreasonably low κ values (not shown), which could only be explained by hygroscopic swelling of the aerosols at ambient humidity by a large factor of up to more than two. A possible reason for this behavior in measurements over the Amazon is that the effective hygroscopicity parameters describing water uptake at sub-saturated conditions can be substantially lower than at supersaturated conditions (Mikhailov et al., 2013). The analysis of this effect on the ASD measurements from PCASP and UHSAS below cloud base requires considerable efforts, which are beyond the scope of this paper. Also, in the case of our flight missions, a major obstacle to the use of the k -Köhler approach is the fact that measuring the CCN(S) spectrum requires a much longer time than the aerosol spectrum, thus the two measurements are not representing the same aerosol sample. This was evident from the variability of the CCN concentrations measured at fixed S with one CCNC column, while measuring the CCN(S) spectrum with the other column during the flights. The lack of these important analyses prevents the use of k -Köhler model estimates for comparison with N_d measurements from cloud probes in the present study.

An estimation of the cloud base droplet concentrations is also possible via the calculation of the maximum supersaturation (S_{max}) at cloud base, relying on the measured N_d and W_b according to Eq. 3 (Pinsky et al. 2012) below:

$$S_{max} = C \cdot W_b^{\frac{3}{4}} \cdot N_d^{-\frac{1}{2}} \quad (3)$$

where C is a coefficient that is determined by cloud base temperature and pressure. Since the combination of $N_{CCN}(S)$ and W_b determines N_d and S_{max} , it is possible to compare the measured and theoretical relationships. Additionally, the estimation of adiabatic cloud droplet concentrations (N_a) from measurements of the vertical profile of cloud drop effective radius (r_e) is another alternative to evaluate the number of droplets nucleated at cloud base (Freud et al., 2011). The definition of r_e is:



$$r_e = \frac{\int N(r) \cdot r^3 dr}{\int N(r) \cdot r^2 dr} \quad (4)$$

105 where N and r are the droplet concentrations and radii, respectively.

Rosenfeld et al. (2014a) have shown that the effective number concentration of droplets at cloud base (N_d^*) can be expressed by a single number, which depends on the effective updraft speed at cloud base (W_b^*). To evaluate whether the measured N_d^* represents the theoretically expected N_d^* based on the independent measurements of $N_{CCN}(S)$ and W_b , it is necessary to find the range of measured W_b^* and N_d^* that fulfills best the closure between the measured and indirectly calculated values. Cloud models represent the number of droplets at cloud base by a single number (Pinsky et al., 2012). Therefore, from a set of N_d measurements at cloud base, an ‘effective’ number of droplets, N_d^* , can be derived, which represents the measurements for a set of clouds formed in the same thermodynamic condition.

115 The droplet size distribution (DSD) spectrum from clouds, i.e. the DSD variability, depends on the stage of cloud development. After nucleation, the cloud droplets in rising cloud parcels grow with height mainly by condensation. Raindrops start forming when r_e reaches 13-14 μm and coalescence becomes efficient (Freud and Rosenfeld, 2012; Rosenfeld and Gutman, 1994). Accurate documentation of the vertical evolution of cloud and rain DSDs is essential for analyzing these types of microphysical processes within clouds. Assessing the quality of DSD measurements by the aircraft probes is thus a necessary task. This assessment can be achieved via comparisons between the cloud water content (CWC) calculated from cloud probe DSDs and the direct measurements of CWC with a hot-wire device (CWCh) for cloud penetrations at different heights (Freud et al., 2008; Rosenfeld et al., 2006). This is done in section 3 while accounting for the dependence of the measurement efficiency of the hot-wire on drop size.

120 Three cloud probes measured the DSDs on board the HALO aircraft during the ACRIDICON-CHUVA campaign (Wendisch et al., 2016). In addition, CWC was measured by a King hot-wire probe (King et al. 1978) installed in the Cloud and Aerosol Spectrometer (CAS-DPOL) probe.

125 Figure 1 illustrates the HALO flight patterns in convective cloud clusters performed in three steps:

- a. Flying below cloud base for measuring $N_{CCN}(S)$;
- b. Flying through cloud base for measuring W_b and DSD;
- c. Conducting vertical profiles in growing convective towers close to their tops, to avoid precipitation that may fall from above. The cloud penetrations during this phase are made in vertical steps of several hundred meters when possible, from cloud base to the anvils.

130 The availability of these measurements collected by the same aircraft provides a unique opportunity to compare the data with model predictions and to test the sensitivity of the results to the differences between the measurements by the cloud probes. Particularly, the validation of physical parameterizations for cloud base of convective clouds over the Amazon basin are on focus in this study. This is the first study that tests the parameterizations against each other with the same data set. In addition, the distributions of the updrafts and N_d at cloud base and their relationships in the context of convective clouds parameterization is account for in this study.

Different approaches are illustrated in the next sections. Section 2 discusses the instrumentation and database used



140 for this study. Section 3 gives an overview on the cloud probe measurements and discusses consistencies and disagreements between the measurements. Section 4 describes the methodologies applied to compare measurements and model results at cloud base.

2. Instrumentation

145 The HALO flights during the ACRIDICON-CHUVA campaign were performed over the Amazon region during September 2014 under different conditions of aerosol concentration and land cover, as shown in Fig. 2 (from Wendisch et al., 2016). This region was chosen for documenting cloud microstructure and precipitation-forming processes during the dry season with high concentrations of CCN, and to contrast these measurements against cleaner conditions that could be found within flight range, as documented previously (Andreae et al., 2004; Artaxo et al., 2002). Additionally, we made use of the fact that Manaus city is located in the central Amazon (3.11 °S; 60.02
150 °W), and that therefore the aerosol perturbation from the Manaus urban plume may increase CCN concentrations by one to two orders of magnitude above the pristine conditions in the background air (Kuhn et al., 2010). This study is done in collaboration with the Green Ocean Amazon experiment – GoAmazon (Martin et al., 2016), which also addressed the aerosol influences on cloud microphysical properties, with special focus on the Manaus urban plume. A comprehensive introduction to airborne instrumentation is given by Wendisch and Brenguier (2013), and in
155 particular of the microphysical instruments involved in this study by Brenguier et al. (2013).

2.1 Cloud condensation nuclei (CCN) measurements

CCN number concentrations were measured on board HALO during ACRIDICON-CHUVA using a two-column CCNC (CCN-200, Column A and B), a continuous-flow longitudinal-thermal-gradient instrument manufactured by
160 Droplet Measurement Technologies (DMT) (Roberts and Nenes, 2005). It measures the CCN number concentration as a function of water vapor supersaturation (S) at a time resolution of 1 Hz. In the instrument, the sampled aerosol particles are exposed to a set supersaturation, and adsorb water depending on their size and chemical composition. Those particles that grow to droplets larger than 1 μm in diameter are counted as CCN at that S . The instrument was calibrated between flights following Rose et al. (2008).

165 Sample air for the aerosol measurements was obtained from two different inlets: (i) the HALO aerosol submicron inlet (HASI), and (ii) the HALO counterflow virtual impactor (HALO-CVI) (Wendisch et al., 2016). The CCN-200 provides the possibility to measure in parallel from both inlets or at two different values of S . In this study, only the aerosol measurements from the HASI inlet have been used. The measurements were done with one column at a constant $S=0.55\%$, while the other was cycling S between 0.2 and 0.55 % with steps every 100 seconds.

170

2.2. Cloud probe measurements

Three cloud probes were operated on board HALO during the measurements in the ACRIDICON-CHUVA campaign. This study focuses on the CAS-DPOL and CCP-CDP probes. The third probe, NIXE-CAS-DPOL was of identical type as CAS-DPOL and is thus not used in this study. The probes' range of measurements is shown in



175 Table 1. In this study, cloud particle concentrations are counted at diameters larger than 3 μm to avoid measurements of haze droplets. This is also in accordance with the similar lower limits of the bins sizes of the CCP-CDP. Details about the cloud probe measurement characteristics are described in the following sections (see also Brenguier et al., 2013).

180 2.2.1 CCP-CDP and CCP-CIP measurements

The Cloud Combination Probe (CCP) combines two detectors, the Cloud Droplet Probe (CDP) and the greyscale Cloud Imaging Probe (CIPgs). The CDP detects forward scattered laser light from cloud particles as they pass through the CDP detection area (Lance et al., 2010), and represents an advanced version of the Forward Scattering Spectrometer Probe (FSSP) (Baumgardner et al., 1985; Dye and Baumgardner, 1984; Korolev et al., 1985; Wendisch
185 et al., 1996). The CIPgs records 2-D shadow-cast images of cloud elements that cross the CIPgs detection region. The overall particle detection size range is 2 to 960 μm when measuring with the CCP. The highest temporal resolution of the CCP measurements is limited to 1Hz. Recent findings concerning the measurement uncertainties of the underwing cloud probes at the comparatively high HALO flight velocities (well above 170 m s^{-1}) provide correction procedures to be applied to the measured raw data to further improve the data quality of the ambient
190 cloud particle number concentrations (Weigel et al., 2016). The robust performance of the specific CCP instrument used in this study, even under extreme conditions, was demonstrated by earlier investigations in tropical convective outflow (Frey et al., 2011), Polar Stratospheric Clouds (PSC) (Molleker et al., 2014), and low-level mixed-phase clouds in the Arctic (Klingebiel et al., 2015). For the CDP sample area of 0.22 mm^2 was used additionally considering an uncertainty of about 10 % (Molleker et al., 2014). The sizing accuracy of the CDP is estimated to be
195 about 10 % for spherical particles and correctly assumed refractive indices.

2.2.2 CAS-DPOL measurements

The CAS-DPOL measures particle size distributions between 0.5 and 50 μm at 1Hz time resolution (Baumgardner et al., 2001). Its measurement principle is developed based on the FSSP-300 (Baumgardner et al., 1985, Korolev et al.,
200 1985), which has been used previously to study the particle size range in ice clouds (Voigt et al., 2010, 2011; Schumann et al., 2011; Jeßberger et al., 2013). The intensity of forward scattered light in the angular range of 4 – 12 $^\circ$ is detected and sorted into 30 size bins. Assuming Mie scattering theory, additional binning into 15 size bins is employed to rule out ambiguities. Polarized backward scattered light is detected to investigate the sphericity and phase of the particles (Baumgardner et al., 2005; Gayet et al., 2012; Järvinen et al., 2016). Number concentrations
205 are derived using the probe air speed measured by the probe. The distribution of time intervals between single particles, recorded for the first 290 particles in each second, did not provide indications of droplet coincidence up to a time resolution of 0.8 μs or a number concentration of 2200 cm^{-3} . After the campaign, the sampling area (SA) which is used to derive the number concentration of particles was characterized by a high-resolution scan with a droplet generator. 250 water droplets of a known, quasi constant size of about 40 μm were dropped at and around
210 the sensitive region perpendicular to the laser beam. The resolution of the droplet generator scan was 25 μm perpendicular to the laser beam and 50 μm along the laser beam. According to the scan, the area of the measured SA



for particle diameters above 3 μm was 0.27 mm^2 , which is 8% higher than the initially reported SA by the manufacturer. The fringe of the area, a region where particles are counted but with low efficiency was about 0.032 mm^2 which represents an uncertainty of 15% of the total SA. Additionally, we estimate an uncertainty of the particle
215 velocity in the CAS sampling tube of 15%, taking into account that particle velocities in the sampling tube may be slowed down or accelerated compared to open path instruments or the Pitot tube velocities at the CAS. This results in a combined uncertainty of the number concentration of 21%.

Calibrations with glass beads of four different sizes (2, 5, 20 and 42 μm) were performed between the flights to monitor the stability of the size bin classification. Difference in the refractive index can be accounted for using the
220 method of e.g. (Rosenberg et al. 2012). The size calibration was stable over the whole campaign. For the purpose of this study mainly the effective diameter range between 10 and 26 μm was evaluated, which employed mainly the lowest amplifier gain stage. For particles up to 20 μm the size calibration did not show any size deviations from the expected values. Larger particles with diameters > 40 μm were shifted towards lower sizes by about 5 μm . We therefore estimate an uncertainty in particle size for particles diameters above 40 μm on the order of 13 to 15 % and
225 less below. The instrument had been installed previously on HALO and the DLR Falcon aircraft during the ML-CIRRUS (Voigt et al., 2016), ACCESS-II, ECLIF, and DACCIWA campaigns.

2.3 Hot-wire CWC measurements

The hot-wire instrument is a King Probe type device that measures the bulk liquid water content (LWC) from 0.01
230 to 3 g m^{-3} in the droplet diameter range of 5 to 50 μm by detecting the power (current) required to maintain a heated wire at a constant temperature of 125 $^{\circ}\text{C}$. The sensitivity of the instrument is reduced for droplets below 10 μm , since smaller particles follow more closely the streamlines around the hot-wire. The instrument was mounted on the CAS-DPOL probe. The accuracy of the King Probe LWC measurement is estimated to be 5 % at 1 g m^{-3} and decreases down to 16 % at 0.2 g m^{-3} , with a sensitivity of 0.02 g m^{-3} (King et al., 1978). For this study, mainly
235 CWC in the range up to 1 g m^{-3} was used.

2.4 Vertical wind speed measurements

The HALO aircraft was equipped with a new meteorological sensor system (Basic HALO Measurement And Sensor System - BAHAMAS) located at the nose of the aircraft (Wendisch et al., 2016). Measurements of updraft
240 speeds during cloud base penetrations during the ACRIDICON-CHUVA campaign have shown maximum vertical wind speeds in the range of 5 m s^{-1} . In these conditions, the uncertainties of W measurements are less than 0.2 m s^{-1} (Mallaun et al., 2015). For a long sequence of measurements at cloud base (> 20 s) these uncertainties become negligible.

245 3. Cloud probe intercomparison

3.1 Method

The validation of convective clouds parameterization requires reliable cloud probe measurements. In this section, we discuss quantitatively the difference in estimated and directly measured CWC and DSDs of the two cloud probes



250 CAS-DPOL and CCP-CDP as well as the hot-wire instrument.

For comparisons between the CWC estimated from the cloud probe DSDs and hot-wire measurements (*CWCh*), we distinguish between spectra that are dominated by condensational growth, and spectra where coalescence becomes important, too. These spectra are separated by the threshold of r_e for significant coalescence, which varies as a function of the drizzle water content (DWC) for 1 second cloud passes (Freud and Rosenfeld, 2012). In addition, droplets with diameters $< 10 \mu\text{m}$ are not captured efficiently by the hot-wire probe, resulting in an underestimation of *CWCh*. The hot-wire device was installed on the CAS-DPOL probe; therefore a better statistical agreement is expected for this probe in comparison with the CCP-CDP. The CCP-CDP was mounted on the other wing, about 15 m away from the hot-wire device (Voigt et al., 2016; Wendisch et al., 2016). Only cloud passes at temperatures greater than $0 \text{ }^\circ\text{C}$ are considered in this intercomparison, to avoid uncertainties of the measurement due to freezing of droplets.

3.2 CWC comparison between cloud probe and hot wire measurements

Comparison of different techniques of cloud water content measurements are challenging regarding the individual instrumental differences, like time resolution, dependence of sensitivity on size and with respect to their target of interest e.g. inhomogeneous, turbulent convective cloud.

For this study we use the hot-wire instrument as a reference to the scattering spectrometer probes since its total water content is derived from a smaller set of physical parameters with an overall uncertainty of maximal 16% as compared to $\sim 30\%$ uncertainty when derived from DSDs.

The calculation of CWC is performed separately with CAS-DPOL and CCP-CDP probes droplet concentrations as follows:

$$CWC = \frac{4\pi}{3} \rho \int N(r)r^3 dr \quad (5)$$

where N is the droplet concentration in m^{-3} , r the droplet radius in m and ρ is the water density (1 g cm^{-3}). The calculation of DWC is done similar to CWC but with different cloud probe and particle size ranges. The DSDs from CCP-CDP and CAS-DPOL are used to calculate the CWC, defined here as the mass of the drops integrated over the diameter range of $3\text{--}50 \mu\text{m}$. Similarly, DSDs from CCP-CIP are used to calculate the DWC, defined here as the mass of the drops integrated over the diameter range of $75\text{--}250 \mu\text{m}$ (Freud and Rosenfeld, 2012).

Figure 3 shows the dependency of calculated r_e as a function of altitude for cloud passes during flights over different conditions of aerosol concentrations (AC13- very polluted, AC18- polluted and AC19 – clean). The probability of rain due to collision and coalescence processes are indicated with dashed lines. It is assumed that rain formation starts when calculated DWC exceeds 0.01 g m^{-3} (Freud and Rosenfeld, 2012). Overall, the figure shows that r_e values increases with altitude. In addition, it shows the effects of aerosol loading, which in higher concentration nucleate a larger number of droplets at cloud base that grows slower as a function of height via condensation. Also, for r_e values $< 9 \mu\text{m}$ the probability of coalescence of droplets is very small and starts to be significant for $r_e > 11 \mu\text{m}$. There is little concern that raindrops precipitate from above when flying near the tops of growing convective clouds (as illustrated at Fig. 1).

The comparison of CWC estimated from the cloud probe data and *CWCh* measured with the hot-wire was



290

performed as a function of r_e , because the measurement efficiency of the hot-wire probe depends on drop size. This type of analysis also provides information about the differences between the two cloud probes regarding the estimated CWCs. Strapp et al. (2003) show that large differences between actual CWC and hot-wire measurements occur when larger drops ($\sim r > 20 \mu\text{m}$) contribute to the cloud water content above 1 g m^{-3} . We therefore limit our analysis to the effective diameter range of $5 \mu\text{m} < r_e < 13 \mu\text{m}$ and compare CWC_h with CWC estimated from the cloud probe DSD only for CWC up to 1 g m^{-3} .

295

The comparison between the mean CWC estimated from the cloud probe DSDs and mean CWC_h are shown as a function of r_e in Fig. 4. The ratio between the CWC_h from the hot-wire measurements and the probe estimates (CWC_r) is also shown (in red color). As the hot-wire has reduced sensitivity for particles with $r_e < 5 \mu\text{m}$, the analysis is performed only for $r_e > 5 \mu\text{m}$.

300

The mean values of CWC estimated from the probes from flights AC08 and AC20 and altitudes between 600 m and 5,000 m generally show an increase with increasing r_e . The CWC uncertainty calculated with CAS-DPOL (CCP-CDP) DSDs is about 22% (10 %) for all measurements. In addition, the uncertainty associated with r_e calculations with CAS-DPOL (CCP-CDP) DSDs is about 14 % (9 %). Within their statistical variability, the CAS-DPOL CWC agrees well with the hot-wire CWC_h over the whole effective radius range (upper panel). The CWC_r for CAS-DPOL (CCP-CDP) is around 1 ± 0.1 (0.8 ± 0.05) for almost all r_e sizes. The comparisons of the CWC_h with the CWC estimated from the CCP-CDP probe (lower panel) shows that CCP-CDP is systematically higher by about 21%. The difference is larger than the standard deviation of the individual measurements. The overall systematic difference (mean of the ratio) in the cloud probe CWC in comparison to CWC_h are 0.04 g m^{-3} (6% in percentage) for CAS-DPOL and 0.11 g m^{-3} (21% in percentage) for CCP-CDP higher than the hot-wire measurements. However, considering the uncertainty of the measurements, all three CWC measurements agree within the uncertainty range (16% and 30%).

305

310

In summary, the CWC_h from the hot-wire agrees better with the CWC derived from CAS-DPOL DSDs. The fact that CCP-CDP was mounted on the opposite wing, while the measurements were performed in very inhomogeneous conditions may account for some of the larger spread between the two instruments (e.g. through the choice of r_e) compared to the CAS-DPOL - hot-wire comparison but cannot explain the systematic offset of the CCP-CDP. In the next sub-section we discuss input parameters for the CWC estimated from the cloud probes like number concentration and size to find an explanation for the observed differences.

315

3.3 Comparing cloud probe N_d and DSDs

320

Figure 5 shows the mean N_d values measured by CAS-DPOL and CCP-CDP (solid line) and the systematic uncertainties of measurements (dashed lines) as a function of r_e for values greater than $5 \mu\text{m}$ (left panel) and the standard deviation of the two cloud probe N_d measurements (right panel). The data is the same used with hot-wire intercomparison. Both probes measure a decrease in number concentration with effective radius, related to coagulation processes in the cloud. Taking into account the increase in CWC with r_e , a reduced number of larger droplets contribute to the enhanced CWC at larger r_e . In general, CAS-DPOL mean N_d agree well (difference lower than 1 %) with mean N_d as CCP-CDP for effective radii between 7 and 11 μm . Statistical significant differences are



325 observed for r_e smaller than 7 μm and above 11 μm . Both probes have similar standard deviation (STDEV) for
different r_e sizes. The STDEV decreases with increasing r_e , varying from $\sim 20 \text{ cm}^{-3}$ to $\sim 10 \text{ cm}^{-3}$.

The two N_d measurements agree within the combined statistical variability and the systematic uncertainties of the
two probe measurements (21% for CAS-DPOL and 10% for CCP-CDP). However, in order to explain the difference
in CWC, we point towards the difference of mean droplet number at $r_e > 11 \mu\text{m}$. Lower number concentrations of the
CAS-DPOL at larger r_e may be related to the shift in droplet radii for particles above 40 μm to smaller sizes that
330 shift the effective radius and the CWC to smaller r_e and smaller CWC. On the other hand, the difference in the size
binning of the two probes may artificially shift particles from higher sizes to lower sizes just by the choice of the bin
boundaries. For the CAS-DPOL, larger bin sizes were chosen in order to avoid ambiguities based on Mie-Lorenz
theory.

The differences in N_d at larger r_e correspond to the enhanced CWC in Fig. 4 and may explain most of the differences
335 in CWC between the probes. The higher number concentration at $r_e < 7 \mu\text{m}$ may be explained by the higher
sensitivity of the CAS-DPOL at smaller sizes. The instrument was built to particularly measure the full spectrum of
aerosol and cloud particles in the size range where aerosols are activated into cloud droplets.

Figure 6a-d shows the mean droplet concentration and CWC as a function of droplet diameter from the cloud
probes. The distributions are shown for four different effective radii to give an impression on the evolution of
particle size and CWC with altitude for the two cloud probes. For r_e between 5 and 6 μm and 8 and 9 μm (Figures
340 6a-b), where collision and coalescence processes are negligible (see Fig. 3), CCP-CDP DSDs are somewhat below
the CAS-DPOL DSDs, revealing an enhanced sensitivity of the CAS-DPOL for smaller particles. For larger r_e
(Figures 6c-d), where coalescence starts and raindrops may be present, CCP-CDP shows slightly larger droplet
concentrations and CWC for diameters $> 15 \mu\text{m}$ in comparison to CAS-DPOL. This may be related to larger
345 droplets that enter the open path instrument sampling area of the CCP-CDP easier than the closed path sampling area
of the CAS-DPOL by falling vertically into the measurement area.

These results suggest that CAS-DPOL and CCP-CDP generally measure similar droplets concentrations in the size
range between 3-50 μm . The observed deviations between the probes could be caused by different inlet
configurations or measurement principles of the two probes, each with individual advantages depending on the
350 measurement target and related size range. However, the differences in DSDs are within the uncertainties of the
measurement and show a much better agreement as compared to earlier measurements at similar conditions (Lance
et al., 2012; Rosenberg et al., 2012).

4. Methodology

355 The following analysis is performed in four steps. Section 4.1 presents the analyses of CCN measurements below
cloud base. Assuming the relation between N_{CCN} and S is given by Eq. 1, the parameters N_0 and the slope k are
calculated from the measurements below cloud base. Section 4.2 describes the estimation of maximum S at cloud
base (S_{max}) based on the measured N_d and W_b there. The co-variability of N_d and W_b is used to estimate the CCN
concentration ($N_{d\text{CCN}}$) by calculating S_{max} according to Eq. 1. This is repeated for the two N_d spectra that were
360 obtained from the two cloud droplet probes. In addition, N_d is estimated by application of the measured W_b spectrum



to Eq. 2 and comparing against the directly measured N_d from the two cloud probes. Section 4.3 outlines the methodology of calculating the effective number of droplets at cloud base from cloud probe measurements (N_d^*). This is done using theoretical considerations based on the estimated values of N_{dT} and N_{dCCN} at cloud base (N_{dT}^* and N_{dCCN}^* , respectively). The exact definitions of all parameters are provided in Section 4.2. Section 4.4 explains the calculation of the estimated adiabatic cloud droplet concentration (N_a), as obtained from the measured vertical profile of cloud drop size distributions.

4.1 CCN measurements below cloud base as a function of S

The measurements of N_{CCN} and S can be parameterized by Eq. 1 and provide N_0 and k (Pruppacher et al., 1998). The typical values of N_0 are about 100 cm^{-3} for pristine conditions, and range from 500 cm^{-3} to several thousand cm^{-3} for polluted continental regions at different levels of aerosol loading. The values of the slope parameter k vary from about 0.3 to 1 in clean and polluted air, respectively (Andreae, 2009).

Two types of CCN measurements were performed: (i) measuring CCN concentration at fixed S ($\sim 0.55\%$) [hereafter referred to S_1 with the corresponding CCN concentration referred as CCN_1] and (ii) measuring CCN concentration at variable S (ranging from 0.2 % to 0.55 %) [hereafter referred to S_2 with the corresponding CCN concentration referred as CCN_2]. Since the CCN_2 measurements were performed at varying S_2 (generally modified every 100 seconds during the flights; hereafter referred as time step), the mean values of these measurements for each time step are used to calculate the N_0 and k parameters in Eq. 1. The flight period of measurements below cloud base in a specific region consisted of several CCN time steps and covered at least one full $N_{CCN}(S)$ spectrum, and is defined as a group of measurements (hereafter referred as a group).

To achieve accurate measurements of CCN_2 as a function of S_2 , a weighting factor calculated from the CCN_1 measurements is applied, as specified in the steps below. Because CCN_1 measures at a fixed supersaturation (S_1), its variability is caused only by changes of total CCN concentration (from aerosol loading) along the flight track (assuming constant size distribution and composition during the measurement group). This is used to correct the $N_{CCN}(S)$ as measured by CCN_2 for these changes of total concentration. The procedure for this analysis is:

1. The mean values of S_1 , S_2 , CCN_1 and CCN_2 measurements (mS_1 , mS_2 , $mCCN_1$ and $mCCN_2$, respectively) are calculated for each time step below cloud base;
2. A factor of aerosol loading (FA) for measurements during a full cycle of S is calculated as follows:

$$FA = \frac{mCCN_1}{TmCCN_1}$$

where $TmCCN_1$ is the mean of all CCN_1 measurements for the group of S cycling. FA provides the deviation of aerosol concentration from the mean for a specific time step in the group;

3. The $mCCN_2$ values for each group are weighted by FA generating normalized $mCCN_2$ values ($NCCN_2 = mCCN_2 / FA$). Then, the $NCCN_2$ are used in combination with mS_2 to fit a power-law-function equation for each group of measurements. From this fit, the values of the parameters N_0 and k in the Twomey equation ($N_{CCN} = N_0 \cdot S^k$) are obtained.



4.2. Estimating S_{max} , N_{dCCN} , and N_{dT}

The number of CCN that nucleate into cloud droplets (N_d) reaches its maximum value near the S_{max} height in the cloud (Pinsky et al., 2012). This level is observed between cloud base and a height up to a few tens of meters above
400 it. The value of S_{max} depends on the vertical velocity at cloud base and on $N_{CCN}(S)$. Therefore, N_d can be used to achieve a closure for N_{dCCN} estimates. N_d is measured with the cloud probes CCP-CDP and CAS-DPOL (N_{cdp} and N_{cas} , respectively). The S_{max} at cloud base was then estimated from N_d and W_b measurements from Eq. 3.

The N_0 and k values that were calculated from measurements below cloud base (as described in Section 4.1) are substituted in Eq. 1 and Eq. 2 for calculating N_{dCCN} and N_{dT} , respectively.

405 The comparisons between N_{dCCN} , N_{dT} and N_d from the cloud probes are discussed in Section 5.2. Measurements of N_d for each probe are considered only for concentrations greater or equal 20 droplets per cubic centimeter, to focus on the convective elements and avoid highly mixed and dissipating portions of the clouds. The time and distance differences between the measurements below cloud base and at cloud base have maximum values of 1 hour and 30 km, respectively. With this consideration, we assume that the N_d measurements at cloud base pertain to the same
410 region as the CCN measurements below cloud base.

According to Twomey (1959), the N_d that should be observed at cloud base increases with W_b (assuming a constant CCN concentration; see Eq. 2). However, at cloud base the variability of W_b and N_d measurements is high due to air turbulence. Since a cloud parcel moves as an eddy with a local W_b that produces a given N_d at cloud base, its continued movement as a turbulent eddy within the cloud adds a large random component to the individual
415 realizations of W_b for a given N_d . These turbulent characteristics greatly reduce the confidence that a given measured W_b within cloud has produced the corresponding measured N_d , and therefore, these measurements are often not well correlated. A suitable method to analyze the relationship between W_b and N_d measurements is the ‘probability matching method’ (PMM) (Haddad and Rosenfeld, 1997). For a set of measurements of W_b and N_d at cloud base, it is expected that larger W_b would produce larger N_d for a given $N_{CCN}(S)$. In a PMM analysis, the same percentiles of
420 updrafts are matched to the same percentiles of N_d (or N_{dCCN} and N_{dT}). As N_d must be produced by positive updrafts (Eq. 2), negative (positive) values of W_b are associated with lower (higher) N_d . This procedure allows identifying the role of W_b (positive) in producing N_d in a set of cloud base measurements. The results of PMM analysis from cloud probes N_d versus W_b , and for estimated N_{dCCN} with N_{dT} are discussed in Section 5.2.1.

4.25 4.3. Estimating W_b^* , N_d^* , N_{dT}^* and N_{dCCN}^*

The formulation of an effective updraft speed at cloud base (W_b^*) is a useful approximation of the updraft spectrum (Rosenfeld et al., 2014a). W_b^* and N_d^* are given in Eqs. (6) and (7):

$$W_b^* = \frac{\int W_b^2}{\int W_b} \quad ; \text{ where } W_b > 0 \quad (6)$$

$$N_d^* = N_d[\text{percentile}(W_b^*)] \quad (7)$$



430 where N_d^* represents the spectrum of N_d at cloud base that matches the same percentile of W_b^* . Figure 7 shows an illustration and example of the estimated value of W_b^* and N_d^* from the CCP-CDP probe for flight AC17. In this case the calculated W_b^* has a value of 1.83 m s^{-1} , which represents the 86th percentile of total measurements at cloud base when sorted by W_b measurements, including negative values. The corresponding percentile of N_d^* (when sorted by N_d) in this case is 1207 cm^{-3} . Another approach for N_d retrieval is the calculation of N_{dT}^* considering W_b^* as the updraft wind speed in Eq. 2. In addition, S_{max} can be estimated by applying the calculated values of W_b^* and N_d^* to Eq. 3. Then, applying the obtained S_{max} to Eq. 1 yields N_{dCCN}^* . The values of the calculated N_{dT}^* and N_{dCCN}^* in this case are $1,175 \text{ cm}^{-3}$ and 915 cm^{-3} , respectively.

4.4. Estimating N_a

440 Another approach for estimating N_d is through the calculation of the adiabatic cloud droplet number concentration, N_a (Freud et al., 2011). The N_a is calculated from CWC and the mean volume droplet mass (M_v) calculations from the cloud probe DSDs obtained during the cloud profiling measurements. This behavior is the outcome of the almost completely inhomogeneous mixing behavior of the clouds with the ambient air (Burnet and Brenguier, 2007; Freud et al., 2011). Recently, Beals et al. (2015) wrote that their "*measurements reveal that turbulent clouds are inhomogeneous, with sharp transitions between cloud and clear air properties persisting to dissipative scales (<1 centimeter). The local droplet size distribution fluctuates strongly in number density but with a nearly unchanging mean droplet diameter*". The dominance of inhomogeneous mixing diminishes when the drops become very large ($r_e > 15 \text{ }\mu\text{m}$) and their evaporation rate becomes more comparable to the mixing rate. This is most evident in those cloud passes where CWC is greater than 25 % of the adiabatic CWC (Freud et al., 2011). The measurements during cloud profiling flights were aimed at penetrating the tops of growing convective towers (as shown at Fig. 1). This was done successfully in the data selected for analysis, as verified by examination of videos recorded by the cockpit camera of HALO. The cloud penetrations occurred mainly near the tops of growing convective cumulus, where mixing is expected to be rather inhomogeneous and little precipitation can fall from above. The validity of this expectation will affect the agreement between N_d and N_a . The N_a is calculated from the slope of CWC and M_v measurements and provides an estimate of the maximum N_d that should be observed within clouds (i.e., the maximum N_d observed at cloud base of growing cumulus clouds). However, this methodology does not account for cloud mixing losses from droplet evaporation and the N_a estimates commonly overestimate the expected N_d by 30 % (Freud et al., 2011). Therefore, in calculating N_a we applied this 30 % correction.

460 5. Results

5.1 CCN measurements below cloud base

The estimation of the N_0 and k parameters in Eq. 1 is made from CCN and S measurements below cloud base. Figure 8 illustrates CCN and S measurements below cloud base for flight AC17 over a deforested region in the central Amazon. The cloud base is located at a height of about 2,300 m. The values of S_1 are constant at $\sim 0.55 \text{ %}$ and the values of S_2 range from 0.2 % to 0.55 %. During these measurements, CCN_1 showed higher values than CCN_2 , which is in agreement with its larger S , and the difference between CCN_1 and CCN_2 increases with decreasing S_2



(e.g., at time $\sim 19:45$ UTC, where CCN_2 values are around 300 cm^{-3} and CCN_1 values are around 700 cm^{-3}). The $mCCN_1$, $mCCN_2$, and $NCCN_2$ for this group of measurements are shown in Fig. 9. In addition, the power fit equation from $NCCN_2$ and mS_2 measurements is shown and the values of N_0 and k are 1015 cm^{-3} and 0.54, respectively. The error estimates of these calculations are shown in Table 2.

This procedure was applied to all cloud profiling flights with measurements of $N_{CCN}(S)$ with variable S below cloud base. The N_0 and k slope parameters for all groups of measurements during the campaign are shown in Fig. 10. The measurements show that for the less polluted conditions, the values of N_0 (k slope) are near 1000 (0.5), while for more polluted conditions, values of N_0 (k slope) greater than 2000 (0.9) are observed. Additionally, the correlation coefficient values for almost all power fit equations are around 0.9. The estimated standard error (STDE) for the N_0 and k parameters and CCN estimates were calculated (as described in Appendix A) for each flight segment and are shown in Table 2. The table shows that the STDE observed for the N_0 and k parameters is lower than 5% of the mean values. For example, the maximum STDE observed for all CCN estimates is $\sim 70 \text{ cm}^{-3}$ in the most polluted case, where N_0 was 4145 cm^{-3} (AC13).

480

5.2 Comparing estimated with measured N_d near cloud base

Cloud base drop concentrations obtained in several different ways were compared. Appendix B summarizes the measurements and theoretical calculations at cloud base. Agreement between these different estimates constitutes a closure. Section 5.2.1 discusses comparisons between cloud probe individual N_d measurements with the corresponding theoretical estimations of N_{dT} and N_{dCCN} . Section 5.2.2 describes the comparisons between estimated N_d^* , N_{dT}^* and N_{dCCN}^* . Section 5.2.3 analyzes the agreement between N_d^* and N_a .

485

5.2.1 Comparison between N_d measurements with estimated N_{dT} and N_{dCCN}

The PMM procedure was applied to the measured W_b and N_d for analyzing the spectrum of N_d , N_{dT} , and N_{dCCN} values near cloud base (as described in Section 4.2). This analytical method makes it possible to identify the role of W_b in producing N_d . A perfect agreement of the values is not expected due to the turbulent nature of the clouds, but the statistical modes of the measurements should have similar values to the theoretical estimation of the same modes of N_{dCCN} and N_{dT} , within their uncertainty range (calculations shown at Appendix C). Figures 11 and 12 show N_{dCCN} , N_{dT} , and N_d values for the two cloud probes as a function of W_b for the cases presented in Table 3. The uncertainties regarding the S_{max} , N_{dCCN} and N_{dT} estimates for measurements at cloud base with both probes (CCP-CDP and CAS-DPOL) are about 20, 30 and 17 %. The values of N_{cas} are with the range of the theoretical expectation of N_{dT} (N_{dCCN}), with higher values of about 6 % (21%) for all flights analyzed (best accuracy in AC11, AC14, and the polluted portion of AC17; Fig. 11e). Slightly higher values ($\sim 15\%$) of N_{cas} as compared to N_{dT} are observed in the maximum values for flight AC14, probably associated with measurements in pollution plumes. Flight AC16 shows measurements slightly lower ($\sim 25\%$) than expected theoretically. A similar behavior of measurements can be observed for the N_{cdp} values (which presents higher values of about 8% in comparison with N_{dT} estimates for all cases), with slight differences with respect to N_{cas} .

495

500

The PMM analysis provided the information that CAS-DPOL and CCP-CDP agree within 30 % to theoretical



estimates for different aerosol conditions, $N_{CCM}(S)$, below cloud base. These results support the analyses concerning the N_d measurements at cloud base that are presented in the next sections.

5.2.2 Comparing estimated N_d^* with N_{dT}^* and N_{dCCN}^*

Assuming that W_b^* represents the updraft velocity for a set of cloud base measurements, the corresponding measured N_d^* from CAS-DPOL and CCP-CDP ideally should have similar values to the estimated N_{dCCN}^* and N_{dT}^* . The uncertainties of N_{dCCN}^* and N_{dT}^* are $\sim 30\%$ and $\sim 17\%$, respectively. Figure 13a shows the values of N_d^* and N_{dT}^* for the different cloud base measurements shown in Figs. 11 and 12. The results indicate that most of N_d^* calculated from CAS-DPOL and CCP-CDP measurements are in agreement with theoretically calculated N_{dT}^* with differences up to 10% (except for measurements from flight AC17 – less polluted case). A similar behavior is observed for comparisons between N_{dCCN}^* and N_d^* (see Fig. 13b), but with differences of a factor of ~ 2 for some cases (AC14 and AC17). Regarding the Twomey formulation (Eq. 2), Figs. 11 and 12 show that: CCP-CDP and CAS-DPOL agree closely with the calculations. Summarized, for this type of closure analysis, the CAS-DPOL and CCP-CDP measurements achieve agreement with theoretical estimates.

5.2.3 Comparing estimated N_d^* with N_a

Another possibility of cloud base closure is via comparison of N_d^* and N_a estimates from N_d measurements in pristine and polluted conditions. In these situations, the estimated values for these parameters must converge. Figure 14a shows the calculated N_a with CCP-CDP probe results from cloud measurements during flight AC17. The estimated N_a in this case is 1496 cm^{-3} , and, considering evaporation losses due to cloud mixing, the expected number of droplets at cloud base is 1047 cm^{-3} after applying the correction by division by 1.3 (Freud et al., 2011). N_d^* for the same flight segment is 1207 cm^{-3} , calculated from CCP-CDP data (see Fig. 7). A close relationship between M_v and r_e as a function of height is shown at Figure 14b. Similar results were found for cloud profile measurements during the other flights.

Values of N_a and N_d^* were calculated for all profile flights and cloud probes, and the results are shown in Fig. 15. The uncertainties of N_a (N_d^*) estimates with CAS-DPOL and CCP-CDP are $\sim 25\%$ (21 %) and $\sim 14\%$ (10%), respectively. The comparisons between the estimated N_a and N_d^* show a linear correlation with correlation coefficients greater than 0.9 for all cloud probes. The linear regression between N_d^* and N_a estimates shows a slope close to one for CAS-DPOL and CCP-CDP. The similarities of N_a , N_d^* values for these several cases supports the methodology to calculate from vertical profile of measured r_e or M_v , (see Fig. 14a-b) the effective number of droplets observed at cloud base of convective clouds.

These results show good agreement with theoretical expectations when done with CAS-DPOL and CCP-CDP. The flights performed in near-pristine and polluted conditions can be distinguished based on the CAS-DPOL estimates from N_d^* and N_a values. For example, in flight AC19 performed over the Atlantic Ocean in clean conditions, the CAS-DPOL estimated values of N_d^* and N_a are $\sim 270\text{ cm}^{-3}$, whereas for flights AC07 and AC11 performed under polluted conditions, the values of N_d^* and N_a are greater than 1000 cm^{-3} . The results from CCP-CDP also showed good agreement between N_d^* and N_a estimates.



For most polluted flights, e.g., AC08, N_d is larger than N_d^* by a factor of ~20-30%. The vertical profiles of the N_d measurements indicate that in these cases the N_d measurements up to 2-3 kilometers above cloud base were larger than those at cloud base. A higher aerosol concentration at these greater heights was also observed in aerosol probe measurements (not shown), suggesting that secondary droplet nucleation was taking place on the most polluted flights. The N_a calculation does not take into account the possibility of new nucleation above cloud base (Freud et al., 2011). Therefore, the assumption of adiabatic growth of droplets via condensation from cloud base to higher levels within cloud leads to an overestimation by ~20-30% of the number of droplets at cloud base when calculating N_a .

The results of Sections 5.2.1 and 5.2.2 highlight that a closure between cloud base measurements and theoretical models was achieved with the CCP-CDP and CAS-DPOL probes. The results from these probes support the methodology to derive N_a based on the rate of r_e growth with cloud depth and with respect to the nature of cloud mixing with the entrained ambient air (Freud et al., 2011). Overall, a perfect relationship between the cloud probe measurements and the theoretical models is not expected. However, a large bias in the measurements would result in a correspondingly large deviation from the calculated values, and closure would not be reached (e.g., when strong secondary nucleation of droplets occurs above cloud base).

6. Conclusions

This work was focused on testing for closures between cloud properties derived from observation-based theoretical estimates and measurements during the ACRIDICON-CHUVA campaign. In addition, liquid water content measurements from a hot-wire device were taken as a reference for the quality assessment of estimated CWC from cloud probe DSDs near cloud base. The intercomparison of the cloud drop size distributions (DSDs) and the cloud water content derived from the different instruments generally shows good agreement within the instrumental uncertainties. The values of N_d near cloud base were compared with their inferred values based on the measured W_b and $N_{CCN}(S)$ spectra. The measured effective droplet numbers (N_d^*) at cloud base were also compared with the theoretically calculated N_{dT}^* and N_{dCCN}^* . In addition, N_d near cloud base was compared with N_a , obtained from the vertical evolution of cloud drop effective radius (r_e) above cloud base. Comparisons of estimated N_d^* with N_{dT}^* and N_{dCCN}^* from the measurements showed good agreement with measurements from CAS-DPOL and CCP-CDP. Similar agreement was observed for comparisons between N_d^* and N_a . The results support the methodology to derive N_a based on the rate of r_e growth with cloud depth and under the assumption that the entrainment and mixing of air into convective clouds is extremely inhomogeneous. In summary, the measurements of $N_{CCN}(S)$ and W_b did reproduce the observed N_d . Furthermore, the vertical evolution of r_e with height reproduced the observation-based adiabatic cloud base drop concentrations, N_a . Our study supports the validity of the parameterizations used, which now can be applied more confidently to simulations and satellite retrievals.

575 Acknowledgements

The first two authors of this study were supported by project BACCHUS European Commission FP7-603445. The generous support of the ACRIDICON-CHUVA campaign by the Max Planck Society, the German Aerospace Center



(DLR), FAPESP (São Paulo Research Foundation), and the German Science Foundation (Deutsche Forschungsgemeinschaft, DFG) within the DFG Priority Program (SPP 1294) “Atmospheric and Earth System Research with the Research Aircraft HALO (High Altitude and Long Range Research Aircraft)” is greatly appreciated. This study was also supported by EU Project HAIC under FP7-AAT-2012-3.5.1-1 and by the German Science Foundation within DFG SPP 1294 HALO by contract no VO1504/4-1 and contract no JU 3059/1-1. The first author also acknowledges the financial support from the Brazilian funding agencies CAPES and CNPq during his Ph.D. degree studies.

585 References

- Andreae, M. O.: Correlation between cloud condensation nuclei concentration and aerosol optical thickness in remote and polluted regions, *Atmos. Chem. Phys.*, 9(2), 543–556, doi:10.5194/acp-9-543-2009, 2009.
- 590 Andreae, M. O., Rosenfeld, D., Artaxo, P., Costa, A. A., Frank, G. P., Longo, K. M. and Silva-Dias, M. A. F.: Smoking rain clouds over the Amazon, *Science*, 303(5662), 1337–42, doi:10.1126/science.1092779, 2004.
- Artaxo, P., Martins, J. V., Yamasoe, M. A., Procópio, A. S., Pauliquevis, T. M., Andreae, M. O., Guyon, P., Gatti, L. V. and Leal, A. M. C.: Physical and chemical properties of aerosols in the wet and dry seasons in Rondônia, Amazonia, *J. Geophys. Res. D Atmos.*, 107(20), 1–14, doi:10.1029/2001JD000666, 2002.
- 595 Baumgardner, D., Strapp, W. and Dye, J. E.: Evaluation of the forward scattering spectrometer probe. Part II: corrections for coincidence and dead-time losses, *J. Atmos. Ocean. Technol.*, 2(4), 626–632, doi:10.1175/1520-0426(1985)002<0626:EOTFSS>2.0.CO;2, 1985.
- 600 Baumgardner, D., Jonsson, H., Dawson, W., O’Connor, D. and Newton, R.: The cloud, aerosol and precipitation spectrometer: a new instrument for cloud investigations, *Atmos. Res.*, 59-60, 251–264, doi:10.1016/S0169-8095(01)00119-3, 2001.
- 605 Baumgardner, D., Chepfer, H., Raga, G. B. and Kok, G. L.: The shapes of very small cirrus particles derived from in situ measurements, *Geophys. Res. Lett.*, 32(1), 1–4, doi:10.1029/2004GL021300, 2005.
- Beals, M. J., Fugal, J. P., Shaw, R. A., Lu, J., Spuler, S. M. and Stith, J. L.: Holographic measurements of inhomogeneous cloud mixing at the centimeter scale, *Science*, 350(6256), 87–90, doi:10.1126/science.aab0751, 2015.
- 610 Brenguier, J. L., Bachalo, W. D., Chuang, P. Y., Esposito, B. M., Fugal, J., Garrett, T., Gayet, J. F., Gerber, H., Heymsfield, A., Kokhanovsky, A., Korolev, A., Lawson, R. P., Rogers, D. C., Shaw, R. A., Strapp, W. and Wendisch, M.: In situ measurements of cloud and precipitation particles in airborne measurements for environmental research: methods and instruments, pp. 225–301., 2013.
- 615 Dye, J. E. and Baumgardner, D.: Evaluation of the forward scattering spectrometer probe. Part I: electronic and optical studies, *J. Atmos. Ocean. Technol.*, 1, 329–344, doi:10.1175/1520-0426(1984)001<0329:EOTFSS>2.0.CO;2, 1984.
- 620 Fan, J., Leung, L. R., Demott, P. J., Comstock, J. M., Singh, B., Rosenfeld, D., Tomlinson, J. M., White, A., Prather, K. A., Minnis, P., Ayers, J. K. and Min, Q.: Aerosol impacts on California winter clouds and precipitation during calwater 2011: local pollution versus long-range transported dust, *Atmos. Chem. Phys.*, 14(1), 81–101, doi:10.5194/acp-14-81-2014f, 2014.
- 625 Burnet, F. and Brenguier, J. L.: Observational study of the entrainment-mixing process in warm convective clouds, *J. Atmos. Sci.*, 64, 1995–2011, doi:10.1175/JAS3928.1, 2007.
- Freud, E. and Rosenfeld, D.: Linear relation between convective cloud drop number concentration and depth for rain initiation, *J. Geophys. Res. Atmos.*, 117(2), 1–13, doi:10.1029/2011JD016457, 2012.



- 630 Freud, E., Rosenfeld, D., Andreae, M. O., Costa, A. A. and Artaxo, P.: Robust relations between CCN and the vertical evolution of cloud drop size distribution in deep convective clouds, *Atmos. Chem. Phys.*, 8(6), 1661–1675, doi:10.5194/acp-8-1661-2008, 2008.
- 635 Freud, E., Rosenfeld, D. and Kulkarni, J. R.: Resolving both entrainment-mixing and number of activated CCN in deep convective clouds, *Atmos. Chem. Phys.*, 11(24), 12887–12900, doi:10.5194/acp-11-12887-2011, 2011.
- 640 Frey, W., Borrmann, S., Kunkel, D., Weigel, R., De Reus, M., Schlager, H., Roiger, A., Voigt, C., Hoor, P., Curtius, J., Krämer, M., Schiller, C., Volk, C. M., Homan, C. D., Fierli, F., Di Donfrancesco, G., Ulanovsky, A., Ravegnani, F., Sitnikov, N. M., Viciani, S., D'Amato, F., Shur, G. N., Belyaev, G. V., Law, K. S. and Cairo, F.: In situ measurements of tropical cloud properties in the West African Monsoon: upper tropospheric ice clouds, mesoscale convective system outflow, and subvisual cirrus, *Atmos. Chem. Phys.*, 11(12), 5569–5590, doi:10.5194/acp-11-5569-2011, 2011.
- 645 Gayet, J.-F., V. Shcherbakov, C. Voigt, U. Schumann, D. Schäuble, P. Jessberger, A. Petzold, A. Minikin, H. Schlager, O. Dubovik, and T. Lapyonok: The evolution of microphysical and optical properties of an A380 contrail in the vortex phase, *Atmos. Chem. Phys.*, 12, 6629–6643, doi:10.5194/acp-12-6629-2012, 2012.
- 650 Ten Hoeve, J. E., Remer, L. A. and Jacobson, M. Z.: Microphysical and radiative effects of aerosols on warm clouds during the Amazon biomass burning season as observed by MODIS: Impacts of water vapor and land cover, *Atmos. Chem. Phys.*, 11(7), 3021–3036, doi:10.5194/acp-11-3021-2011, 2011.
- 655 Järvinen, E., Schnaiter, M., Mioche, G., Jourdan, O., Shcherbakov, V., Costa, A., Afchine, A., Krämer, M., Heidelberg, F., Jurkat, T., Voigt, C., Schlager, H., Nichman, L., Gallagher, M., Hirst, E., Schmitt, C., Bansemer, A., Heymsfield, A., Lawson, P., U. Tricoli, Pfeilsticker, K., Vochezer, P., Möhler, O. and Leisner, T.: Quasi-spherical ice in convective clouds, *J. Atmos. Sci.*, doi:10.1175/JAS-D-15-0365.1, 2016.
- 660 Jeßberger, P., Voigt, C., Schumann, U., Sölch, I., Schlager, H., Kaufmann, S., Petzold, A., Schäuble, D. and Gayet, J. F.: Aircraft type influence on contrail properties, *Atmos. Chem. Phys.*, 13(23), 11965–11984, doi:10.5194/acp-13-11965-2013, 2013.
- Jiang, H. and Feingold, G.: Effect of aerosol on warm convective clouds: aerosol-cloud-surface flux feedbacks in a new coupled large eddy model, *J. Geophys. Res.*, 111(D1), D01202, doi:10.1029/2005JD006138, 2006.
- 665 King, W. D., Parkin, D. A. and Handsworth, R. J.: A hot-wire liquid water device having fully calculable response characteristics, *J. Appl. Meteorol.*, 17(12), 1809–1813, doi:10.1175/1520-0450(1978)017<1809:AHWLWD>2.0.CO;2, 1978.
- 670 Klingebiel, M., De Lozar, A., Molleker, S., Weigel, R., Roth, A., Schmidt, L., Meyer, J., Ehrlich, A., Neuber, R., Wendisch, M. and Borrmann, S.: Arctic low-level boundary layer clouds: In situ measurements and simulations of mono- and bimodal supercooled droplet size distributions at the top layer of liquid phase clouds, *Atmos. Chem. Phys.*, 15(2), 617–631, doi:10.5194/acp-15-617-2015, 2015.
- 675 Kohler, M.: Explicit prediction of ice clouds in general circulation models., 1999.
- Korolev, A. V., Makarov, Y. E. and Novikov, V. S.: On the calibration of cloud particle counter FSSP-, *Trans. Cent. Aerol. Obs.*, 158(January 1985), 43–49, 1985.
- 680 Kuhn, U., Ganzeveld, L., Thielmann, A., Dindorf, T., Schebeske, G., Welling, M., Sciare, J., Roberts, G., Meixner, F. X., Kesselmeier, J., Lelieveld, J., Kolle, O., Ciccioli, P., Lloyd, J., Trentmann, J., Artaxo, P. and Andreae, M. O.: Impact of Manaus city on the Amazon Green Ocean atmosphere: ozone production, precursor sensitivity and aerosol load, *Atmos. Chem. Phys.*, 10(19), 9251–9282, doi:10.5194/acp-10-9251-2010, 2010.
- 685 Lance, S.: Coincidence errors in a cloud droplet probe (CDP) and a cloud and aerosol spectrometer (CAS), and the improved performance of a modified CDP, *J. Atmos. Ocean. Technol.*, 29(10), 1532–1541, doi:10.1175/JTECH-D-11-00208.1, 2012.



- 690 Lance, S., Brock, C. A., Rogers, D. and Gordon, J. A.: Water droplet calibration of the cloud droplet probe (CDP) and in-flight performance in liquid, ice and mixed-phase clouds during ARCPAC, *Atmos. Meas. Tech.*, 3(6), 1683–1706, doi:10.5194/amt-3-1683-2010, 2010.
- 695 Machado, L. A. T., Silva Dias, M. A. F., Morales, C., Fisch, G., Vila, D., Albrecht, R., Goodman, S. J., Calheiros, A. J. P., Biscaro, T., Kummerow, C., Cohen, J., Fitzjarrald, D., Nascimento, E. L., Sakamoto, M. S., Cunningham, C., Chaboureau, J. P., Petersen, W. A., Adams, D. K., Baldini, L., Angelis, C. F., Sapucci, L. F., Salio, P., Barbosa, H. M. J., Landulfo, E., Souza, R. A. F., Blakeslee, R. J., Bailey, J., Freitas, S., Lima, W. F. A. and Tokay, A.: The CHUVA project: how does convection vary across Brazil?, *Bull. Am. Meteorol. Soc.*, 95(9), 1365–1380, doi:10.1175/BAMS-D-13-00084.1, 2014.
- 700 Mallaun, C., Giez, A. and Baumann, R.: Calibration of 3-D wind measurements on a single-engine research aircraft, *Atmos. Meas. Tech.*, 8(8), 3177–3196, doi:10.5194/amt-8-3177-2015, 2015.
- 705 Martin, S. T., Artaxo, P., Machado, L. A. T., Manzi, A. O., Souza, R. A. F., Schumacher, C., Wang, J., Andreae, M. O., Barbosa, H. M. J., Fan, J., Fisch, G., Goldstein, A. H., Guenther, A., Jimenez, J. L., Pöschl, U., Silva Dias, M. A., Smith, J. N. and Wendisch, M.: Introduction: Observations and modeling of the Green Ocean Amazon (GoAmazon2014/5), *Atmos. Chem. Phys.*, 16(8), 4785–4797, doi:10.5194/acp-16-4785-2016, 2016.
- Mikhailov, E., Vlasenko, S., Rose, D. and Pöschl, U.: Mass-based hygroscopicity parameter interaction model and measurement of atmospheric aerosol water uptake, *Atmos. Chem. Phys.*, 13(2), 717–740, doi:10.5194/acp-13-717-2013, 2013.
- 710 Molleker, S., Borrmann, S., Schlager, H., Luo, B., Frey, W., Klingebiel, M., Weigel, R., Ebert, M., Mitev, V., Matthey, R., Woiwode, W., Oelhaf, H., Dörnbrack, A., Stratmann, G., Groß, J. U., Günther, G., Vogel, B., Müller, R., Krämer, M., Meyer, J. and Cairo, F.: Microphysical properties of synoptic-scale polar stratospheric clouds: in situ measurements of unexpectedly large HNO₃-containing particles in the arctic vortex, *Atmos. Chem. Phys.*, 14(19), 10785–10801, doi:10.5194/acp-14-10785-2014, 2014.
- 715 Petters, M. D. and Kreidenweis, S. M.: A single parameter representation of hygroscopic growth and cloud condensation nucleus activity, *Atmos. Chem. Phys.*, 1961–1971, doi:10.5194/acp-7-1961-2007, 2007.
- 720 Pinsky, M., Khain, A., Mazin, I. and Korolev, A.: Analytical estimation of droplet concentration at cloud base, *J. Geophys. Res. Atmos.*, 117(17), 1–14, doi:10.1029/2012JD017753, 2012.
- 725 Pöhlker, M. L., Pöhlker, C., Klimach, T., Angelis, I. H. de, Barbosa, H. M. J., Brito, J., Samara Carbone, Cheng, Y., Chi, X., Ditas, F., Ditz, R., Gunthe, S. S., Kesselmeier, J., Könemann, T., Lavrič, J. V., Martin, S. T., Moran-Zuloaga, D., Rose, D., Saturno, J., Su, H., Thalman, R., Walter, D., Wang, J., Wolff, S., Artaxo, P., Andreae, M. O. and Pöschl, U.: Long-term observations of atmospheric aerosol, cloud condensation nuclei concentration and hygroscopicity in the Amazon rain forest – Part 1: size-resolved characterization and new model parameterizations for CCN prediction, *Atmos. Chem. Phys.*, (July), doi:10.5194/acp-2016-519, 2016.
- 730 Pruppacher, H. R., Klett, J. D. and Wang, P. K.: Microphysics of clouds and precipitation, *Aerosol Sci. Technol.*, 28, 381–382, doi:10.1080/02786829808965531, 1998.
- 735 Reutter, P., Su, H., Trentmann, J., Simmel, M., Rose, D., Gunthe, S. S., Wernli, H., Andreae, M. O. and Pöschl, U.: Aerosol- and updraft-limited regimes of cloud droplet formation: influence of particle number, size and hygroscopicity on the activation of cloud condensation nuclei (CCN), *Atmos. Chem. Phys.*, 9(18), 7067–7080, doi:10.5194/acp-9-7067-2009, 2009.
- Roberts, G. C. and Nenes, a.: A continuous-flow streamwise thermal-gradient CCN chamber for atmospheric measurements, *Aerosol Sci. Technol.*, 39(3), 206–221, doi:10.1080/027868290913988, 2005.
- 740 Rose, D., Gunthe, S. S., Mikhailov, E., Frank, G. P., Dusek, U., Andreae, M. O., and Pöschl, U., Calibration and measurement uncertainties of a continuous-flow cloud condensation nuclei counter (DMT-CCNC): CCN activation



- of ammonium sulfate and sodium chloride aerosol particles in theory and experiment: *Atmos. Chem. Phys.*, 8, 1153–1179, 2008.
- 745 Rosenberg, P. D., Dean, A. R., Williams, P. I., Dorsey, J. R., Minikin, A., Pickering, M. A., and Petzold, A.: Particle sizing calibration with refractive index correction for light scattering optical particle counters and impacts upon PCASP and CDP data collected during the Fennec campaign, *Atmos. Meas. Tech.*, 5, 1147–1163, doi:10.5194/amt-5-1147-2012, 2012.
- 750 Rosenfeld, D. and Gutman, G.: Retrieving microphysical properties near the tops of potential rain clouds by multispectral analysis of AVHRR data, *Atmos. Res.*, 34(1-4), 259–283, doi:10.1016/0169-8095(94)90096-5, 1994.
- Rosenfeld, D., Woodley, W. L., Krauss, T. W. and Makitov, V.: Aircraft microphysical documentation from cloud base to anvils of hailstorm feeder clouds in Argentina, *J. Appl. Meteorol. Climatol.*, 45(9), 1261–1281, doi:10.1175/JAM2403.1, 2006.
- 755 Rosenfeld, D., Lohmann, U. and Raga, G.: Flood or drought: how do aerosols affect precipitation?, *Science* (80-.), 321(September), 1309–1313, 2008.
- 760 Rosenfeld, D., Fischman, B., Zheng, Y., Goren, T. and Giguzin, D.: Combined satellite and radar retrievals of drop concentration and CCN at convective cloud base, *Geophys. Res. Lett.*, 41(9), 3259–3265, doi:10.1002/2014GL059453, 2014a.
- 765 Rosenfeld, D., Chemke, R., Prather, K., Suski, K., Comstock, J. M., Schmid, B., Tomlinson, J. and Jonsson, H.: Polluting of winter convective clouds upon transition from ocean inland over central California: contrasting case studies, *Atmos. Res.*, 135–136, 112–127, doi:10.1016/j.atmosres.2013.09.006, 2014b.
- Schumann, U., Mayer, B., Gierens, K., Unterstrasser, S., Jessberger, P., Petzold, A., Voigt, C. and Gayet, J.-F.: Effective radius of ice particles in cirrus and contrails, *J. Atmos. Sci.*, 68, 300–321, doi:10.1175/2010JAS3562.1, 2011.
- 770 Silva Dias, M. A. F., Petersen, W., Silva Dias, P. L., Cifelli, R., Betts, A. K., Longo, M., Gomes, A. M., Fisch, G. F., Lima, M. A., Antonio, M. A. and Albrecht, R. I.: A case study of convective organization into precipitating lines in the southwest Amazon during the WETAMC and TRMM-LBA, *J. Geophys. Res. D Atmos.*, 107(20), doi:10.1029/2001JD000375, 2002.
- Stephens, G.: The parameterization of radiation for numerical weather prediction and climate models, *Mon. Weather Rev.*, 1984.
- 780 Strapp, J. W., Oldenburg, J., Ide, R., Lilie, L., Bacic, S., Vukovic, Z., Oleskiw, M., Miller, D., Emery, E. and Leone, G.: Wind tunnel measurements of the response of hot-wire liquid water content instruments to large droplets, *J. Atmos. Ocean. Technol.*, 20(6), 791–806, doi:10.1175/1520-0426(2003)020<0791:WTMOTR>2.0.CO;2, 2003.
- 785 Twomey, S.: The nuclei of natural cloud formation part II: the supersaturation in natural clouds and the variation of cloud droplet concentration, *Geofis. Pura e Appl.*, 43(1), 243–249, doi:10.1007/BF01993560, 1959.
- 790 Voigt, C., Schumann, U., Jurkat, T., Schäuble, D., Schlager, H., Petzold, A., Gayet, J. F., Krämer, M., Schneider, J., Borrmann, S., Schmale, J., Jessberger, P., Hamburger, T., Lichtenstern, M., Scheibe, M., Gourbeyre, C., Meyer, J., Kübbeler, M., Frey, W., Kalesse, H., Butler, T., Lawrence, M. G., Holzäpfel, F., Arnold, F., Wendisch, M., Döpelheuer, A., Gottschaldt, K., Baumann, R., Zöger, M., Sölch, I., Rautenhaus, M. and Dörnbrack, A.: In-situ observations of young contrails - overview and selected results from the CONCERT campaign, *Atmos. Chem. Phys.*, 10(18), 9039–9056, doi:10.5194/acp-10-9039-2010, 2010.
- 795 Voigt, C., Schumann, U., Jessberger, P., Jurkat, T., Petzold, A., Gayet, J. F., Krmer, M., Thornberry, T. and Fahey, D. W.: Extinction and optical depth of contrails, *Geophys. Res. Lett.*, 38(11), doi:10.1029/2011GL047189, 2011.
- Voigt, C., Schumann, U., Minikin, A., Abdelmonem, A., Afchine, A., Borrmann, S., Boettcher, M., Buchholz, B.,



800 Bugliaro, L., Costa, A., Curtius, J., Dollner, M., Dörnbrack, A., Dreiling, V., Ebert, V., Ehrlich, A., Fix, A., Forster, L., Frank, F., Fütterer, D., Giez, A., Graf, K., Groß, J., Groß, S., Heimerl, K., Heinold, B., Hüneke, T., Järvinen, E., Jurkat, T., Kaufmann, S., Kenntner, M., Klingebiel, M., Klimach, T., Kohl, R., Krämer, M., Krisna, T., Luebke, A., Mayer, B., Mertes, S., Molleker, S., Petzold, A., Pfeilsticker, K., Port, M., Rapp, M., Reutter, P., Rolf, C., Rose, D., Sauer, D., Schäfler, A., Schlage, R., Schnaiter, M., Schneider, J., Spelten, N., Spichtinger, P., Stock, P., Walsler, A., Weigel, R., Weinzierl, B., Wendisch, M., Werner, F., Wernli, H., Wirth, M., Zahn, A., Ziereis, H. and Zöger, M.: ML-CIRRUS - the airborne experiment on natural cirrus and contrail cirrus with the high-altitude long-range research aircraft HALO, Bull. Am. Meteorol. Soc., doi:10.1175/BAMS-D-15-00213.1, 2016.

810 Weigel, R., Spichtinger, P., Mahnke, C., Klingebiel, M., Afchine, A., Petzold, A., Krämer, M., Costa, A., Molleker, S., Jurkat, T., Minikin, A. and Borrmann, S.: Thermodynamic correction of particle concentrations measured by underwing probes on fast flying aircraft, Atmos. Meas. Tech., 9, 5135-5162, doi:10.5194/amt-9-5135, 2016.

Wendisch, M., Keil, A. and Korolev, A. V.: FSSP characterization with monodisperse water droplets, J. Atmos. Ocean. Technol., 13(6), 1152–1165, doi:10.1175/1520-0426(1996)013<1152:FCWMWD>2.0.CO;2, 1996.

815 Wendisch, M., and J.-L. Brenguier (Eds.), 2013: Airborne measurements for environmental research: methods and instruments. Wiley-VCH Verlag GmbH & Co. KGaA, Weinheim, Germany. ISBN: 978-3-527-40996-9. 655 pp., doi:10.1002/9783527653218

820 Wendisch, M., Pöschl, U., Andreae, M. O., Machado, L. A. T., Albrecht, R., Schlager, H., Rosenfeld, D., Martin, S. T., Abdelmonem, A., Afchine, A., Araújo, A., Artaxo, P., Aufmhoff, H., Barbosa, H. M. J., Borrmann, S., Braga, R., Buchholz, B., Cecchini, M. A., Costa, A., Curtius, J., Dollner, M., Dorf, M., Dreiling, V., Ebert, V., Ehrlich, A., Ewald, F., Fisch, G., Fix, A., Frank, F., Fütterer, D., Heckl, C., Heidelberg, F., Hüneke, T., Jäkel, E., Järvinen, E., Jurkat, T., Kanter, S., Kästner, U., Kenntner, M., Kesselmeier, J., Klimach, T., Knecht, M., Kohl, R., Kölling, T., Krämer, M., Krüger, M., Krisna, T. C., Lavric, J. V., Longo, K., Mahnke, C., Manzi, A. O., Mayer, B., Mertes, S., Minikin, A., Molleker, S., Münch, S., Nillius, B., Pfeilsticker, K., Pöhlker, C., Roiger, A., Rose, D., Rosenow, D., Sauer, D., Schnaiter, M., Schneider, J., Schulz, C., de Souza, R. A. F., Spanu, A., Stock, P., Vila, D., Voigt, C., Walsler, A., Walter, D., Weigel, R., Weinzierl, B., Werner, F., Yamasoe, M. A., Ziereis, H., Zinner, T. and Zöger, M.: The ACRIDICON-CHUVA campaign: studying tropical deep convective clouds and precipitation over Amazonia using the new german research aircraft HALO, Bull. Am. Meteorol. Soc., 160128144638003, doi:10.1175/BAMS-D-14-00255.1, 2016.

830

Appendix - A

Calculating STDE CCNmax and STDE CCNmin

835 The N_0 and k parameters standard errors (STDE) are associated with the statistical uncertainty of the power law function fit. To compute the STDE for the CCN estimates the uncertainties of S (~10%) are considered. Then, the maximum and the minimum STDE values expected for the CCN estimates are calculated as follows:

Maximum STDE

$$STDE\ CCN_{max} = \frac{[(N_0 + SD \cdot N_0) \cdot (S_i \cdot 1.1)^{k+SD \cdot k}] - N_0 \cdot S_i^k}{\sqrt{N}} \quad (A1)$$

840

where:

The averaging is done on $I=1:N$.

N is the number of $NCCN_2$ cases for each group of measurements.

$SD \cdot N_0$ is the statistical standard deviation of N_0 ;



- 845 SD.k is the statistical standard deviation of k ;
 S_i is the supersaturation in each step, forced to have the maximum value (multiplied by 1.1).

Minimum STDE

850

$$STDE\ CCNmin = \frac{N_0 \cdot S_i^k - [(N_0 - SD \cdot N_0) * (S_i \cdot 0.9)^{k-SD \cdot k}]}{\sqrt{N}} \quad (A2)$$

where:

The averaging is done on $I=1:N$.

N is the number of $NCCN_2$ cases for each group of measurements.

$SD \cdot N_0$ is the statistical standard deviation of N_0 ;

- 855 SD.k is the statistical standard deviation of k ;
 S_i is the supersaturation in each step, forced to have the minimum value (multiplied by 0.9).

Appendix – B

Summary of the measurements and theoretical calculations at cloud base:

- 860 1) N_d - based on probe measurement;
 2) N_a - based on vertical profile of r_e ;
 3) $S_{max} - S$ substituting N_d and W_b in Eq. 3.
 4) N_{dT} - Obtained from substituting in Eq. 2 W_b and $N_{CCN}(S)$ parameters (k and N_0);
 5) N_{dCCN} - Obtained from substituting S_{max} and $N_{CCN}(S)$ parameters in Eq. 1.
 865 6) W_b^* - Obtained from Eq. 5.
 7) $N_d^*, N_{dT}^*, N_{dCCN}^* - N_{db}, N_{dT}, N_{dCCN}$ that match W_b^* .

Appendix – C

870 *Calculating uncertainty for N_{dT}*

The calculation is similar of *STDE CCNmax* and *STDE CCNmin* considering also the W_b uncertainty (assumed the maximum; 0.2 m s^{-1}). Therefore, the maximum and the minimum uncertainty values of N_{dT} are calculated as follow:

Maximum uncertainty

$$N_{dTmax} = \frac{0.88 \cdot [N_{0max}^{2/kmax+2} \cdot (0.07W_{bmax}^{1.5})]^{kmax} - 0.88 \cdot [N_0^{2/k+2} \cdot (0.07W_b^{1.5})]^{k}}{\sqrt{N}} \quad (C1)$$

875 *Minimum uncertainty*

$$N_{dTmin} = \frac{0.88 \cdot [N_0^{2/k+2} \cdot (0.07W_b^{1.5})]^{k} - 0.88 \cdot [N_{0min}^{2/kmin+2} \cdot (0.07 \cdot W_{bmin}^{1.5})]^{kmin}}{\sqrt{N}} \quad (C2)$$



where:

$$N_{0max} = N_0 + SD.N_0$$

$$N_{0min} = N_0 - SD.N_0$$

$$k_{max} = k + SD.k$$

880 $k_{min} = k - SD.k$

$$W_{bmax} = W_b + 0.2$$

$$W_{bmin} = W_b - 0.2; \text{ for } W_b \text{ greater than } 0.2$$

N is the number of N_d measurements for each group of measurements.

885 *Calculating uncertainty for N_{dCCN}*

The calculation is similar of *STDE CCNmax* and *STDE CCNmin* considering also the S_{max} uncertainty (assumed the maximum; 20 %). Therefore, the maximum and the minimum uncertainty values of N_{dCCN} are calculated as follow:

$$N_{dCCNmax} = \frac{[N_{0max}^{2/k_{max}+2} \cdot (S_{max} \cdot 1.2)]^{\frac{k_{max}}{k_{max}+2}} - [N_0^{2/k+2} \cdot (S_{max} \cdot 1.2)]^{\frac{k}{k+2}}}{\sqrt{N}} \quad (C3)$$

890

$$N_{dCCNmin} = \frac{[N_0^{2/k+2} \cdot (S_{max} \cdot 1.2)]^{\frac{k}{k+2}} - [N_{0min}^{2/k_{min}+2} \cdot (S_{max} \cdot 0.8)]^{\frac{k_{min}}{k_{min}+2}}}{\sqrt{N}} \quad (C4)$$

where:

$$N_{0max} = N_0 + SD.N_0$$

$$N_{0min} = N_0 - SD.N_0$$

895 $k_{max} = k + SD.k$

$$k_{min} = k - SD.k$$

N is the number of N_d measurements for each group of measurements.

Figure captions

900 Figure 1. Flight patterns below and in convective clouds during the ACRIDICON-CHUVA campaign.

Figure 2. HALO flight tracks during the ACRIDICON-CHUVA experiment. The flight numbers are indicated on the right (from Wendisch et al., 2016).

905 Figure 3. Cloud droplet effective radius (r_e) as a function of altitude for clouds over clean (Flight AC19 - blue color squares), polluted (Flight AC18 - green color triangles) and very polluted (Flight AC13 - brown color diamonds) environments. Dashed lines indicate the probability of rain from the coalescence process expressed in percentage on the top of the graphic.



Figure 4. Mean cloud water content from the hot-wire measurements and estimated from the cloud probes (CCP-CDP and CAS-DPOL from top to bottom, respectively) as a function of effective radius (r_e) size (left panel). The ratios between the hot-wire liquid water content and the cloud water content derived from each probe are shown in red (CWC_r). The total uncertainty for each probe and the hot-wire measurements are shown by the dotted lines. The number of cases (black continuous line), hot-wire measurement standard deviations (dashed black line), and probe CWC standard deviations (dashed colored line) for each r_e size are shown in the right panels.

910

Figure 5. Mean cloud droplet concentrations for CAS-DPOL and CCP-CDP as a function of effective radius (r_e) (left panel). The systematic error for each probes shown by the dashed line. The right panel indicates the standard deviation in cm^{-3} of each probe concentration as a function of r_e . The probes are identified by colors as shown in the top of the panels. The sample for each probe is the same as shown in Figure 3.

915

Figure 6. (left) Mean cloud droplet concentration (solid lines) and (right) cloud water content as a function of droplet diameter in the left and right panels, respectively, for a) $5 \mu\text{m} < r_e < 6 \mu\text{m}$; b) $8 \mu\text{m} < r_e < 9 \mu\text{m}$; c) $11 \mu\text{m} < r_e < 12 \mu\text{m}$; d) $12 \mu\text{m} < r_e < 13 \mu\text{m}$. The probes are identified by colors as shown at the top of the panels. The dashed lines indicate the uncertainty range of mean cloud droplet concentration and cloud water content values as a function of droplet diameter.

920

Figure 7. a) Frequency histogram for vertical wind speed (W_b) from cloud base measurements on flight AC17 (labeled on the left ordinate). The blue line indicates the cumulative probability function of W_b (labeled on the right ordinate). The cyan arrow indicates the value of W_b^* (1.83 m s^{-1}), which represents the 86th percentile of the W spectra; b) Similar for the cloud droplet concentrations measured with the CCP-CDP probe. The cyan line indicates the N_d^* value (1207 cm^{-3}) at the 86th percentile in the N_d spectra. The indicated time is in UTC and shows the time of the first cloud penetration at cloud base and the total number of 1-s measured cloud data points.

925

Figure 8. CCN_1 (red dots) and CCN_2 (black dots) measurements for a segment of flight AC17 on 27 September 2014. The abscissa shows the measurement time in UTC. The blue line indicates the altitude in meters above sea level and is labeled on the left ordinate (as well as CCN_1 and CCN_2). S_1 and S_2 measurements in % are indicated by the orange and green lines, respectively (both are labeled on the right ordinate). Cyan dots on the blue line indicate cloud penetrations (i.e., when cloud droplets concentrations are greater than 20 cm^{-3}). In this case, cloud base heights were observed around 2,300 meters above ground.

930

Figure 9. A comparison of the CCN spectra derived from the two CCN counter columns on board the HALO aircraft during flight AC17. Black (blue) smaller dots indicate CCN_1 (CCN_2) measurements for each second. Large diamonds in black (blue) indicate the $mCCN_1$ ($mCCN_2$) for each time step of measurements. The orange large diamonds indicate the $NCCN_2$ values, which are used to fit the power law equation of the group of measurements, which is shown at the lower right corner of the plot. The standard error for CCN spectra derived is shown at Table 2.

935

Figure 10. CCN spectra as measured on board the HALO aircraft during cloud profiling flights. Diamonds indicate the $NCCN_2$ values, which are used to fit the power law equation of the group of measurements. The colors indicate the group of measurements and match the legend on the right side of the plot. The legend indicates the flight number; the initial time of group measurements; the period of measurements in seconds; the power law fit and the correlation coefficient of the data. The standard errors for each CCN spectra derived are shown at Table 2.

940



- Figure 11a-f. N_{dCCN} , S , N_{dT} and N_d values are presented as a function of the cloud base updrafts (W_b). This plot is based on the ‘probability matching method’ (PMM), using same percentiles for W_b and N_d (N_{dCCN} or N_{dT}). The values of N_{dCCN} , N_{dT} and N_d are shown the left y-axis, those of S on the right y-axis. The black dashed lines are the N_{dT} uncertainties. The gray solid (dashed) lines are the N_{dCCN} values (uncertainties). The effective updraft W_b^* for each flight segment is shown by the cyan line. The data are based on the CAS-DPOL probe. The time, period of measurements (sample size in seconds), and $CCN(S)$ equation are shown on the top of the figures
- Figure 12a-d. Same as Figure 7 for the CCP-CDP probe. No data were available for flight AC16. The CCP-CDP malfunctioned in flight AC13 during the cloud base measurements.
- Figure 13. a) N_d^* versus N_{dT}^* calculated with W_b^* from cloud base data shown in Figures 7-8. The CAS-DPOL values are indicated by plus symbols (+) and the CCP-CDP values are indicate by circles (o). The colors indicate each flight segment (legend in the right side of the plot). Error bars indicates the uncertainties of variables estimates. Lines show the 1:1 and 1:2 relationships between N_{dT}^* versus N_d^* for each probe (dotted line – CCP-CDP; solid line – CAS-DPOL); b) Same for N_d^* versus N_{dCCN}^* .
- Figure 14 a). Mean volume drop mass (M_v) versus liquid water content from the CCP-CDP measurements for adiabatic fraction greater than 0.25 (LWC_a). Vaues are shown with different colors labeled as a function of height in kilometers above sea level (indicated by the colorbar on the right side of the graphic). The slope of the linear equation is the estimated N_a (i.e., 1496 cm^{-3}); b) M_v versus re as a function of height in kilometers above sea level (indicated by the colorbar on the right side of the graphic).
- Figure 15. N_d^* versus N_a measured with CAS-DPOL and CCP-CDP (indicated on the top of panels) for profile flights during the ACRIDICON-CHUVA campaign. The color of the dots is associated with the flight number shown at the right side of the panels. Error bars indicates the uncertainties of variables estimates. The linear regression equation and the correlation coefficient R are shown in the top of each panel.

Table captions

Table 1. Cloud probe size intervals and central bin diameters during HALO flights.

- Table 2. Estimates of N_p and k below cloud base and their standard error (STDE) for each case study. Maximum and minimum STDE (STDE CCN_{max} and STDE CCN_{min} , respectively) for the CCN measurements are calculated considering errors in the supersaturation measurements ($\sim 10\%$). The details about the calculation of these uncertainties are given in Appendix A.

- Table 3. List of case studies for measurements below cloud base. The duration of measurements is given in seconds, starting at the initial time indicated. An asterisk indicates those flights where the two probes provided at least 20 seconds of measurements at cloud base. The data can be from different cloud passes in the same region of measurements below cloud base.



Tables

Table 1. Cloud probe size intervals and central bin diameters during HALO flights.

980

Cloud Probe	Size interval	Number of bins	Central bin diameter (μm)
CCP-CDP	3-50 μm	14	3.8, 6.1, 8.7, 10.9, 13.5, 17.1, 19.7, 22.5, 25.9, 28.3, 31.7, 36.6, 40.7, 44.2
CAS-DPOL	3-50 μm	10	3.9, 6, 10.8, 17.3, 22.3, 27.4, 32.4, 37.4, 42.4, 47.4

Table 2. Estimates of N_0 and k below cloud base and their standard error (STDE) for each case study. Maximum and minimum STDE (STDE CCN_{max} and STDE CCN_{min} , respectively) for the CCN measurements are calculated considering errors in the supersaturation measurements ($\sim 10\%$). The details about the calculation of these uncertainties are given in Appendix A.

985

Flight	Time	N_0	k	STDE N_0	STDE k	STDE CCN_{max} [cm^{-3}]	STDE CCN_{min} [cm^{-3}]
AC11	14:58:21	1985	0.73	81.6	0.035	25.5	24.8
AC11	17:38:20	2927	1.14	82.8	0.032	43.9	43.8
AC12	15:56:00	1764	0.3	71.4	0.046	19.0	22.7
AC13	16:29:01	4145	0.92	64.7	0.016	69.7	54.8
AC14	15:21:40	1509	0.97	44.8	0.028	24.7	18.9
AC15	13:33:35	2209	0.94	70.4	0.038	47.4	31.2
AC16	20:21:40	1966	0.67	69.5	0.029	26.5	21.2
AC17	16:50:50	2743	0.72	38.7	0.013	31.9	30.5
AC17	19:38:20	1015	0.54	18.5	0.018	10.7	9.4



990

Table 3. List of case studies for measurements below cloud base. The duration of measurements is given in seconds, starting at the initial time indicated. An asterisk indicates those flights where the two probes provided at least 20 seconds of measurements at cloud base. The data can be from different cloud passes in the same region of measurements below cloud base.

Measurements below cloud base			
Flight	Date	Initial time (UTC)	Period of analysis (s)
AC11	16/09/2014	14:58:21	593
AC11*	16/09/2014	17:38:20	710
AC12	18/09/2014	15:56:00	440
AC13*	19/09/2014	16:29:01	722
AC14*	21/09/2014	15:21:40	800
AC15	23/09/2014	13:33:35	555
AC16	25/09/2014	20:21:40	550
AC17*	27/09/2014	16:50:50	831
AC17*	27/09/2014	19:38:20	840

995



Figures

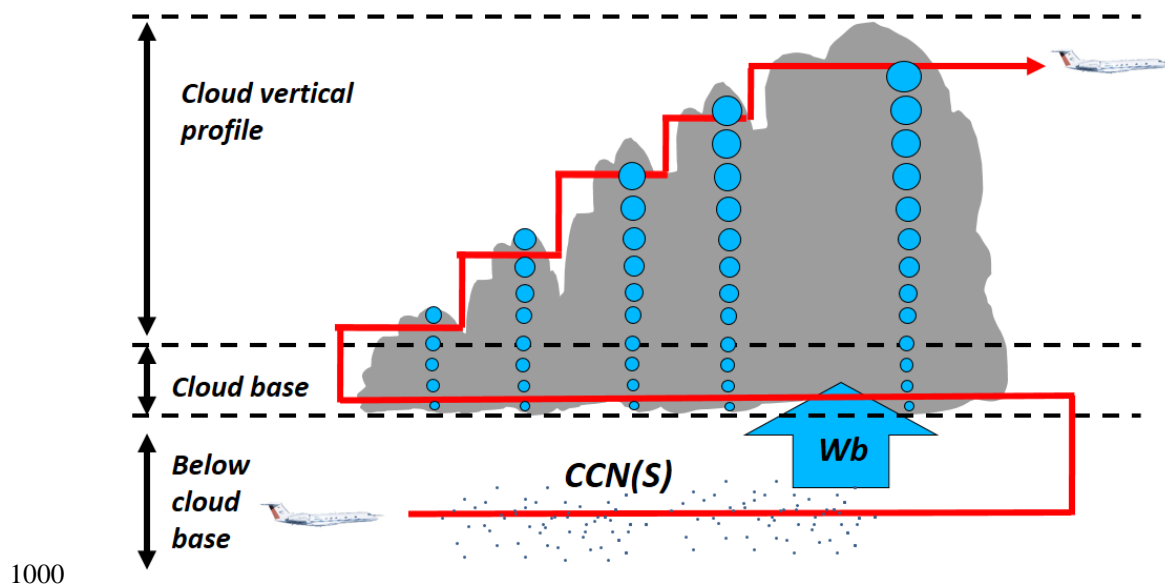


Figure 1. Flight patterns below and in convective clouds during the ACRIDICON-CHUVA campaign.

1005

1010

1015

1020

1025

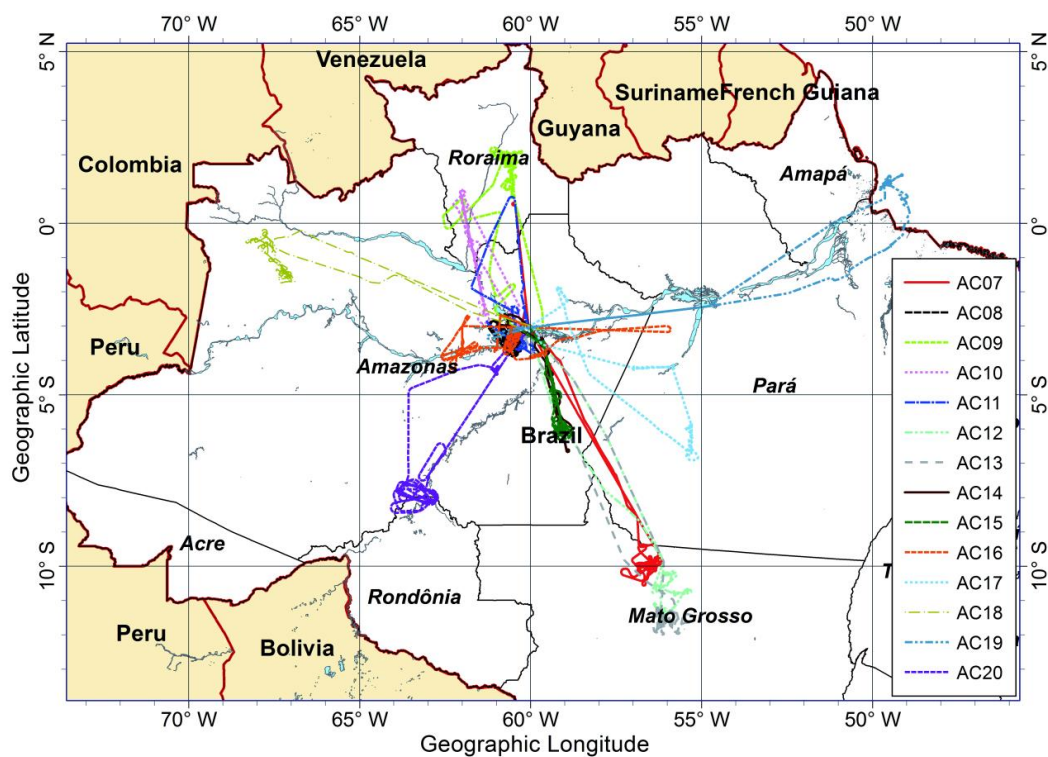


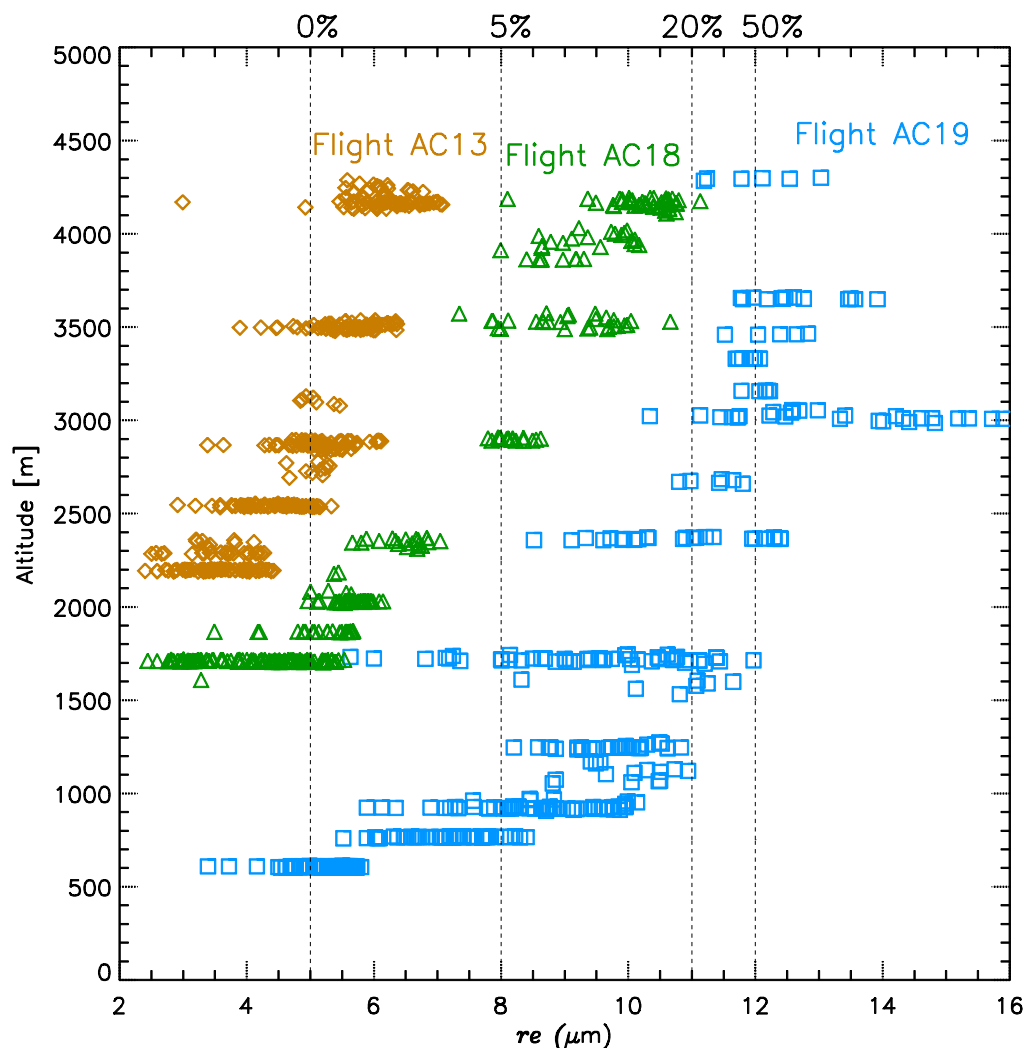
Figure 2. HALO flight tracks during the ACRIDICON-CHUVA experiment. The flight numbers are indicated on the right (from Wendisch et al., 2016).

1030

1035

1040

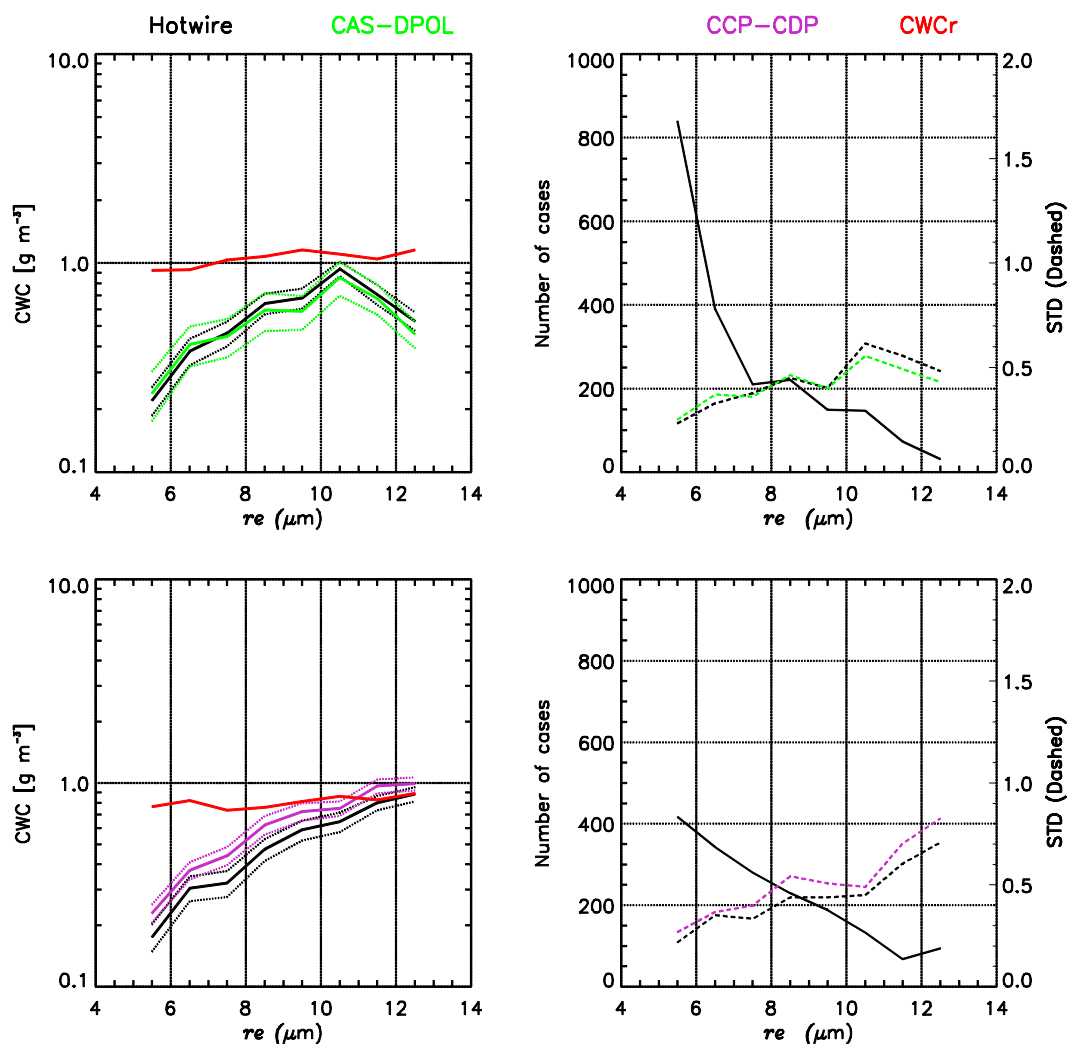
1045



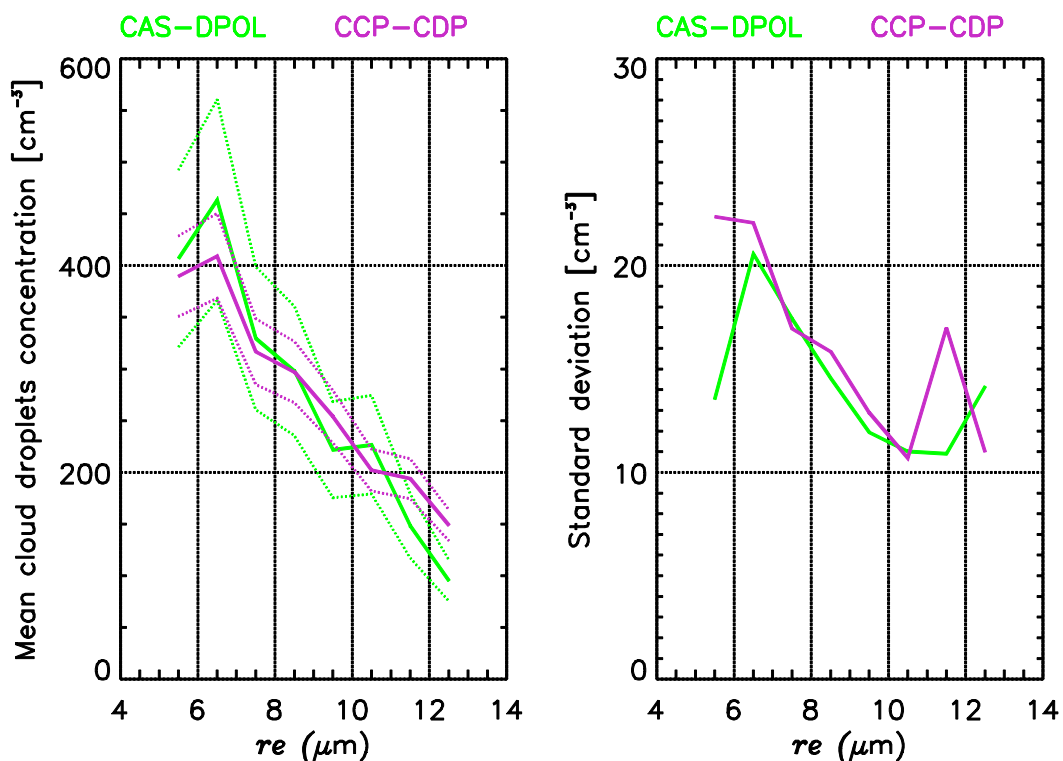
1050

Figure 3. Cloud droplet effective radius (r_e) as a function of altitude for clouds over clean (Flight AC19 - blue color squares), polluted (Flight AC18 - green color triangles) and very polluted (Flight AC13 - brown color diamonds) environments. Dashed lines indicate the probability of rain from the coalescence process expressed in percentage on the top of the graphic.

1055



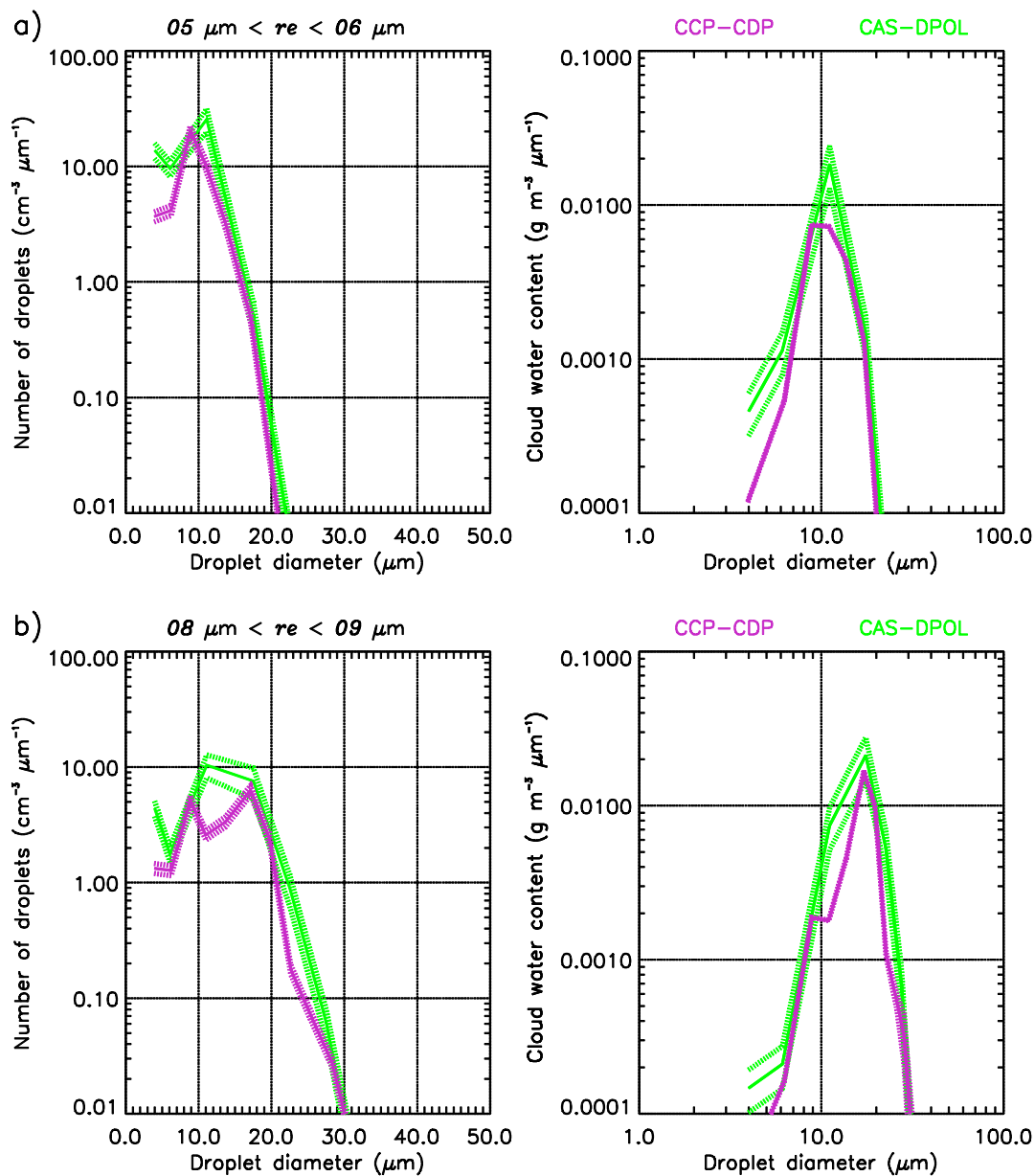
1060 Figure 4. Mean cloud water content from the hot-wire measurements and estimated from the cloud probes (CCP-CDP
 1065 and CAS-DPOL from top to bottom, respectively) as a function of effective radius (r_e) size (left panel). The ratios between
 the hot-wire liquid water content and the cloud water content derived from each probe are shown in red (CWC_r). The
 total uncertainty for each probe and the hot-wire measurements are shown by the dotted lines. The number of cases
 (black continuous line), hot-wire measurement standard deviations (dashed black line), and probe CWC standard
 deviations (dashed colored line) for each r_e size are shown in the right panels.



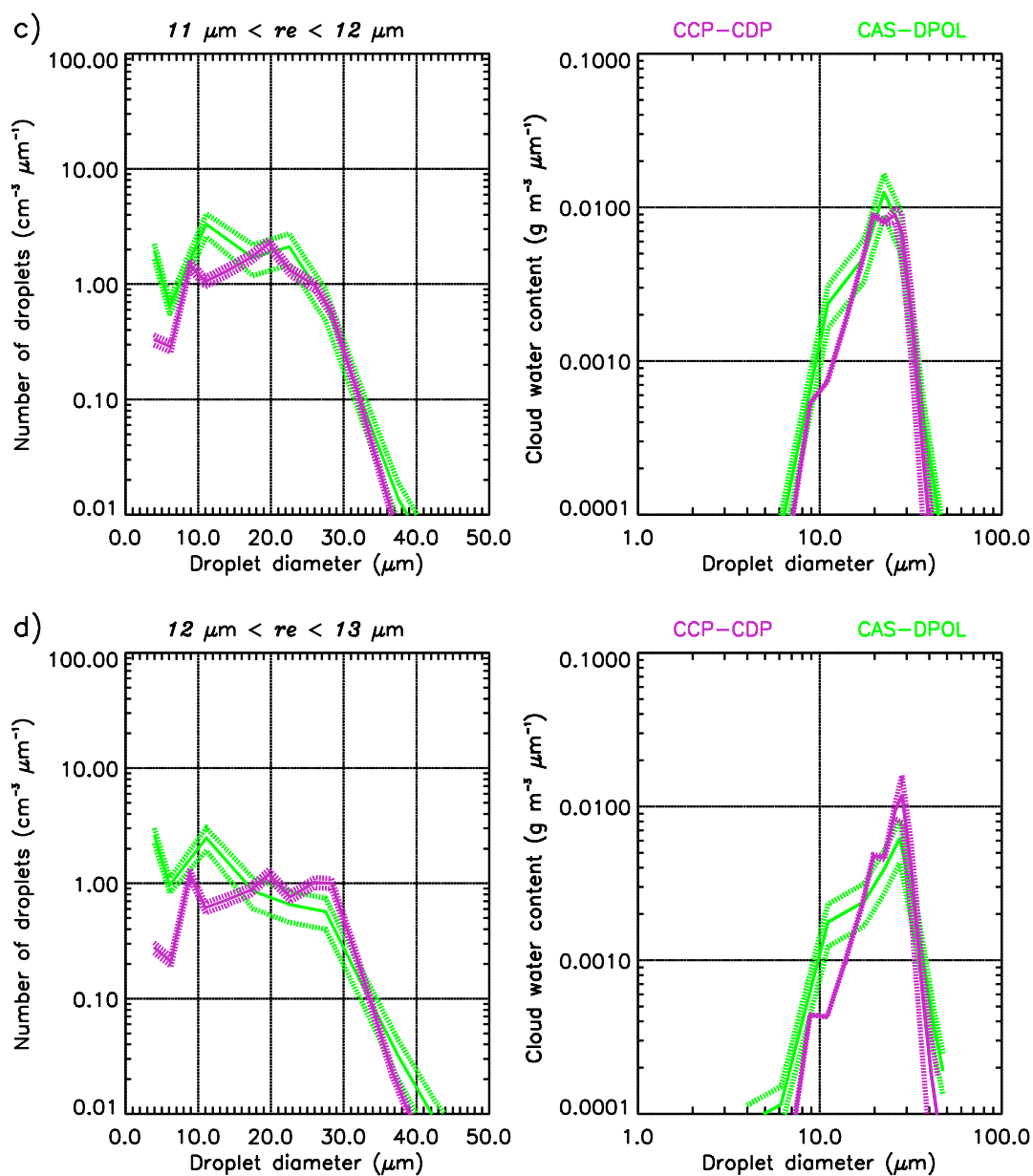
1070 Figure 5. Mean cloud droplet concentrations for CAS-DPOL and CCP-CDP as a function of effective radius (r_e) (left panel). The systematic error for each probes shown by the dashed line. The right panel indicates the standard deviation in cm^{-3} of each probe concentration as a function of r_e . The probes are identified by colors as shown in the top of the panels. The sample for each probe is the same as shown in Figure 3.

1075

1080



1085

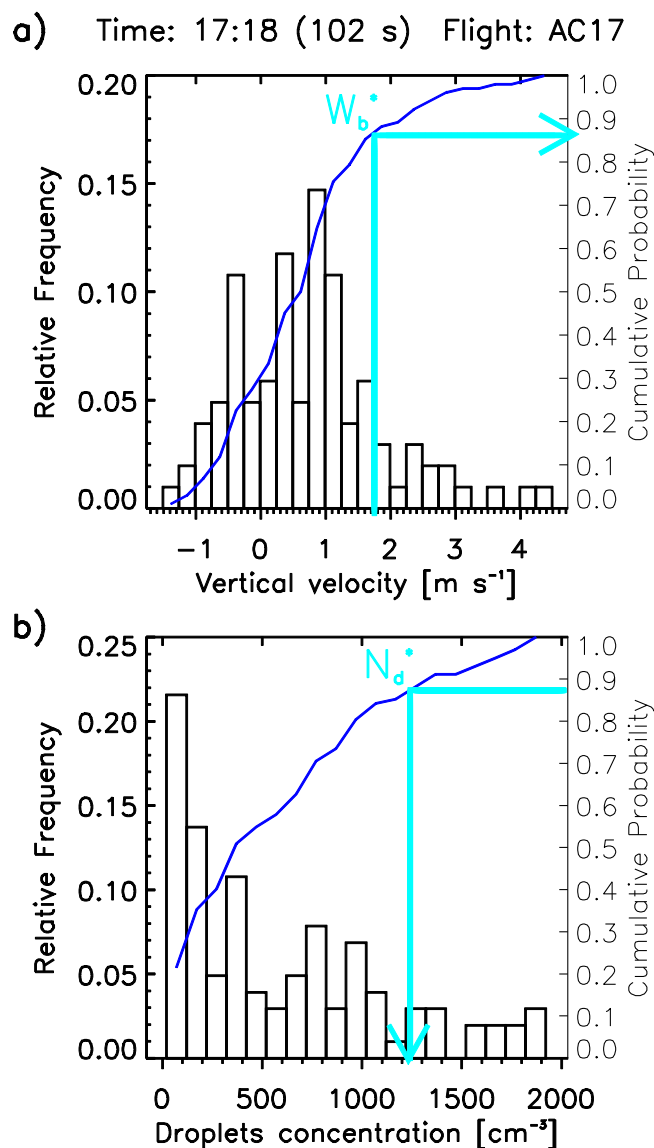


1090

1095

1100

Figure 6. (left) Mean cloud droplet concentration (solid lines) and (right) cloud water content as a function of droplet diameter in the left and right panels, respectively, for a) $5 \mu\text{m} < r_e < 6 \mu\text{m}$; b) $8 \mu\text{m} < r_e < 9 \mu\text{m}$; c) $11 \mu\text{m} < r_e < 12 \mu\text{m}$; d) $12 \mu\text{m} < r_e < 13 \mu\text{m}$. The probes are identified by colors as shown at the top of the panels. The dashed lines indicate the uncertainty range of mean cloud droplet concentration and cloud water content values as a function of droplet diameter.

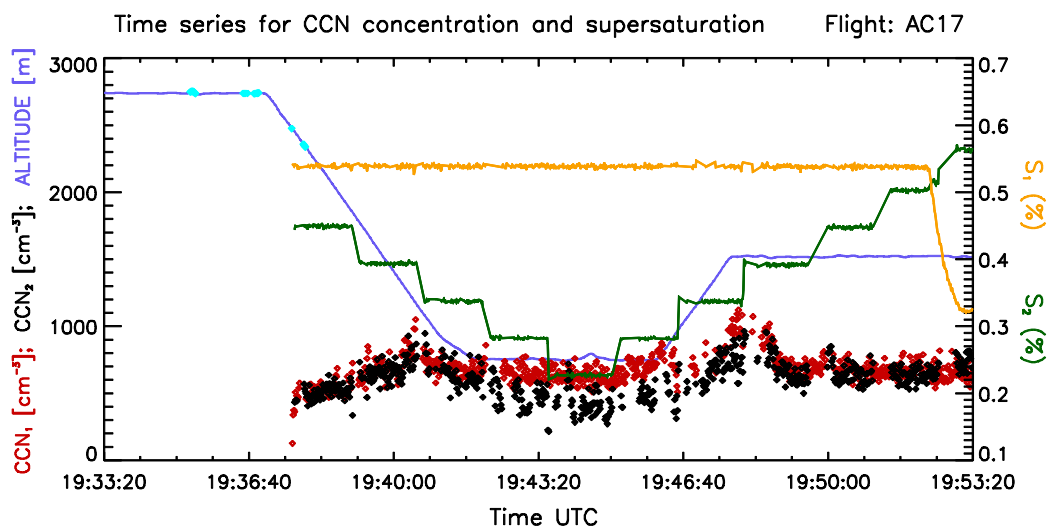


1105

Figure 7. a) Frequency histogram for vertical wind speed (W_b) from cloud base measurements on flight AC17 (labeled on the left ordinate). The blue line indicates the cumulative probability function of W_b (labeled on the right ordinate). The cyan arrow indicates the value of W_b^* (1.83 m s^{-1}), which represents the 86th percentile of the W spectra; b) Similar for the cloud droplet concentrations measured with the CCP-CDP probe. The cyan line indicates the N_d^* value (1207 cm^{-3}) at the 86th percentile in the N_d spectra. The indicated time is in UTC and shows the time of the first cloud penetration at cloud base and the total number of 1-s measured cloud data points.



1110

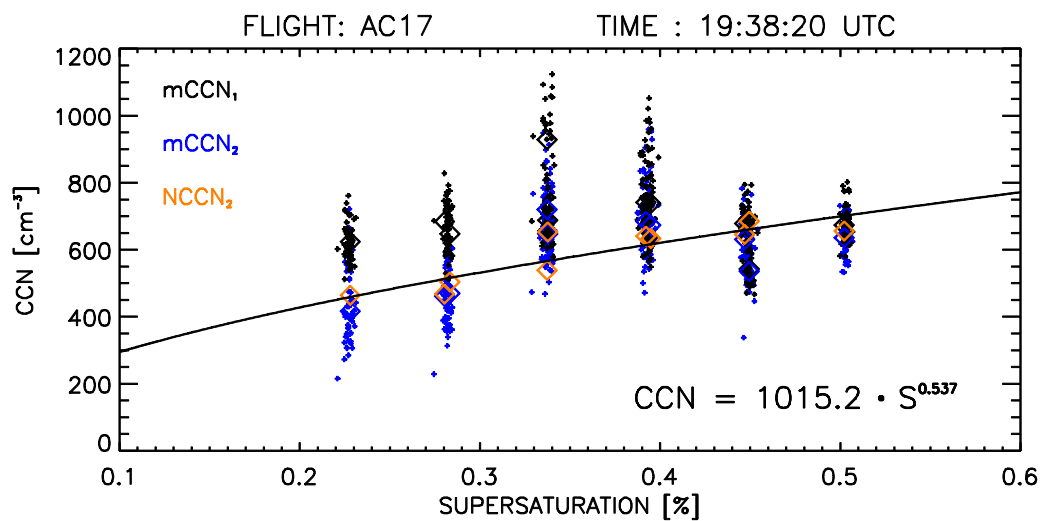


1115

Figure 8. CCN_1 (red dots) and CCN_2 (black dots) measurements for a segment of flight AC17 on 27 September 2014. The abscissa shows the measurement time in UTC. The blue line indicates the altitude in meters above sea level and is labeled on the left ordinate (as well as CCN_1 and CCN_2). S_1 and S_2 measurements in % are indicated by the orange and green lines, respectively (both are labeled on the right ordinate). Cyan dots on the blue line indicate cloud penetrations (i.e., when cloud droplets concentrations are greater than 20 cm^{-3}). In this case, cloud base heights were observed around 2,300 meters above ground.

1120

1125



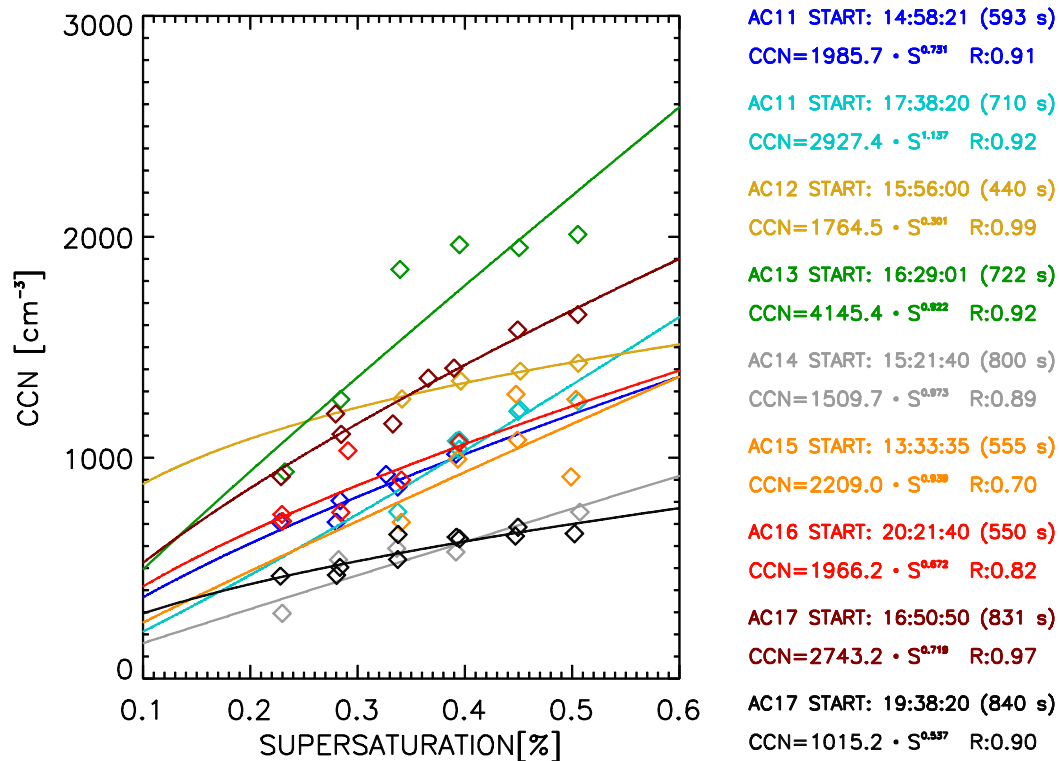
1130

Figure 9. A comparison of the *CCN* spectra derived from the two *CCN* counter columns on board the HALO aircraft during flight AC17. Black (blue) smaller dots indicate *CCN*₁ (*CCN*₂) measurements for each second. Large diamonds in black (blue) indicate the *mCCN*₁ (*mCCN*₂) for each time step of measurements. The orange large diamonds indicate the *NCCN*₂ values, which are used to fit the power law equation of the group of measurements, which is shown at the lower right corner of the plot. The standard error for *CCN* spectra derived is shown at Table 2.

1135

1140

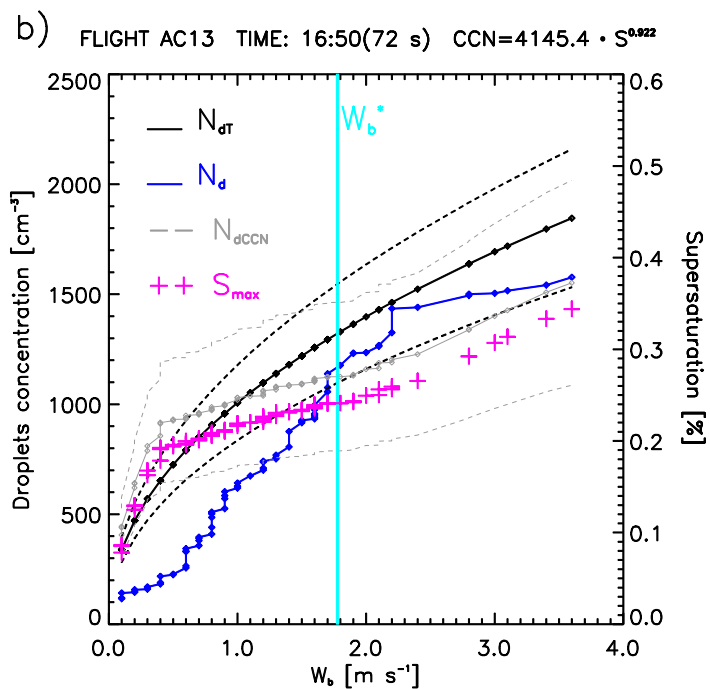
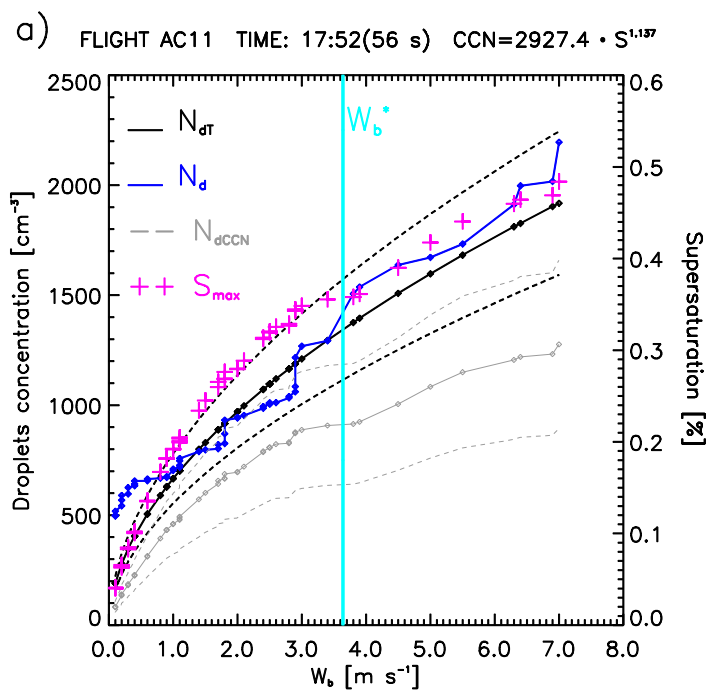
1145

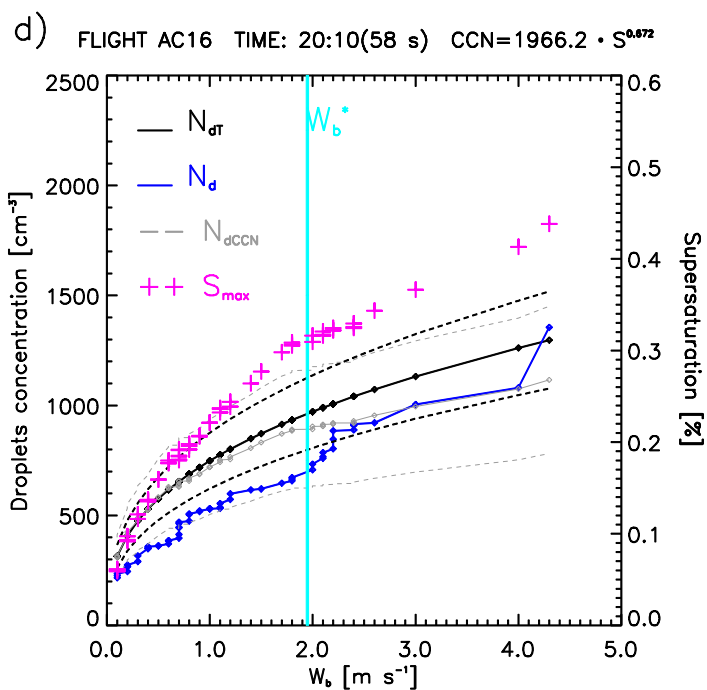
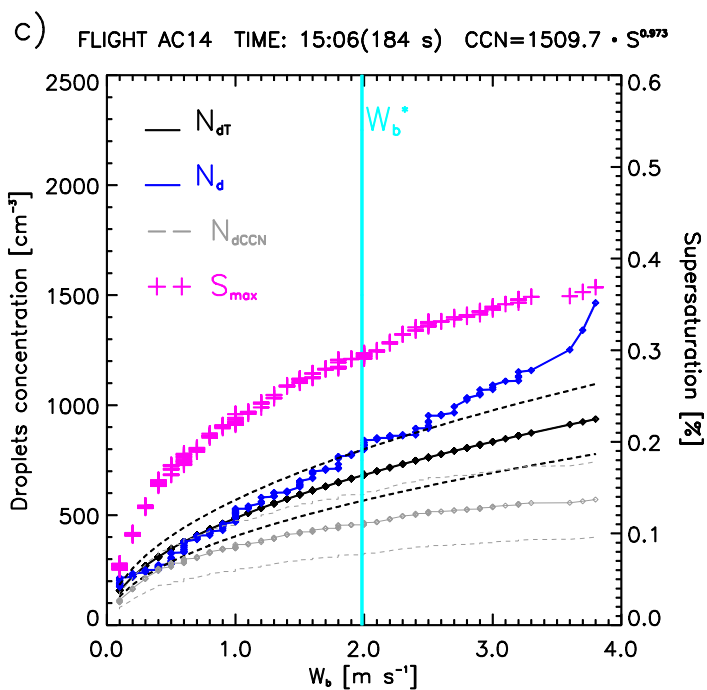


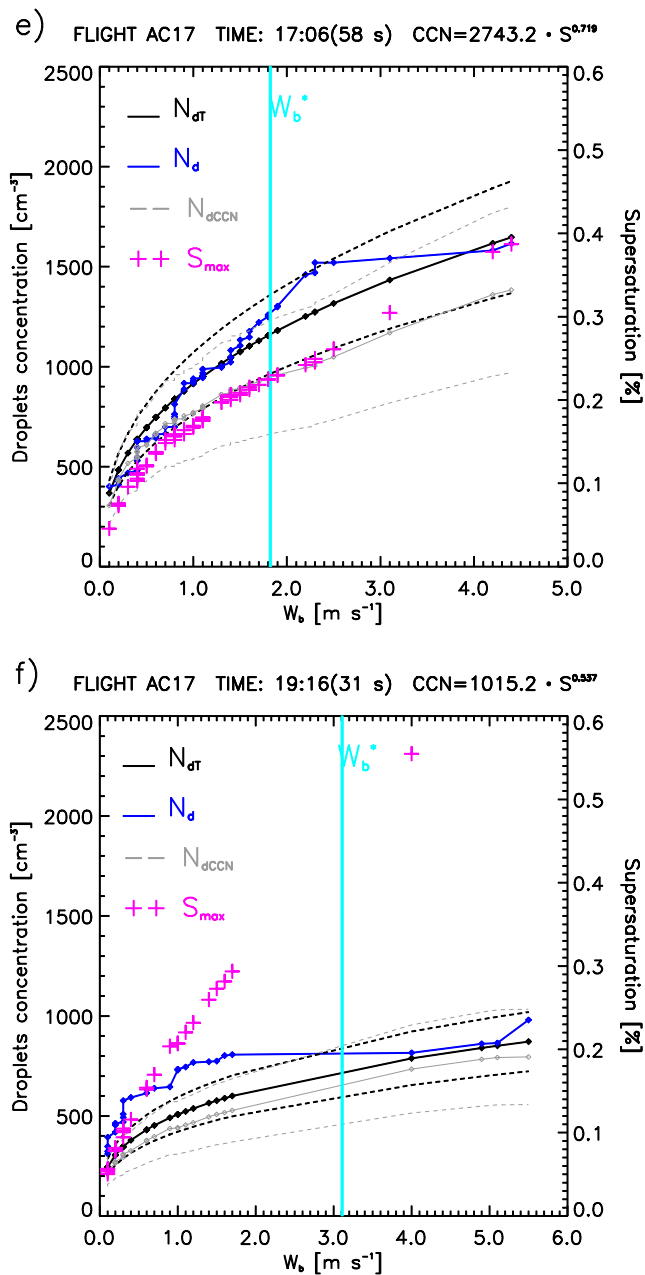
1150 Figure 10. CCN spectra as measured on board the HALO aircraft during cloud profiling flights. Diamonds indicate the $NCCN_2$ values, which are used to fit the power law equation of the group of measurements. The colors indicate the group of measurements and match the legend on the right side of the plot. The legend indicates the flight number; the initial time of group measurements; the period of measurements in seconds; the power law fit and the correlation coefficient of the data. The standard errors for each CCN spectra derived are shown at Table 2.

1155

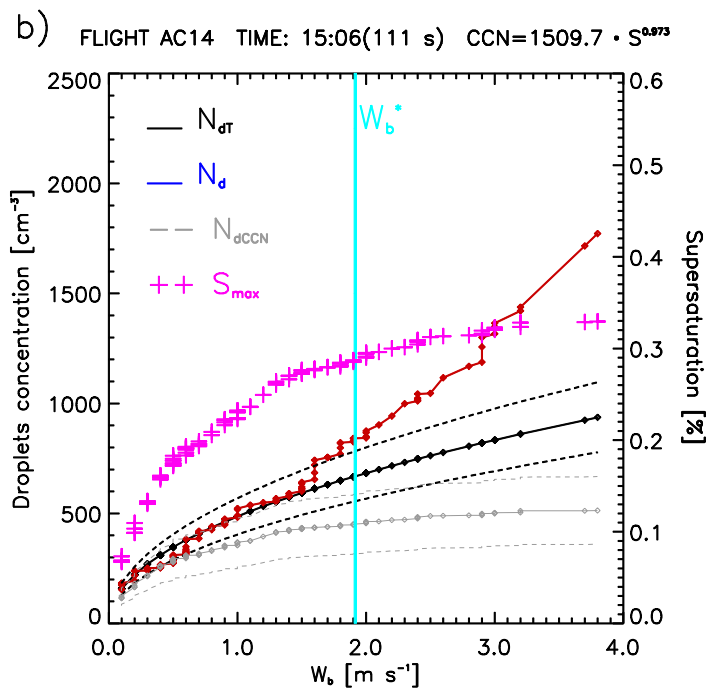
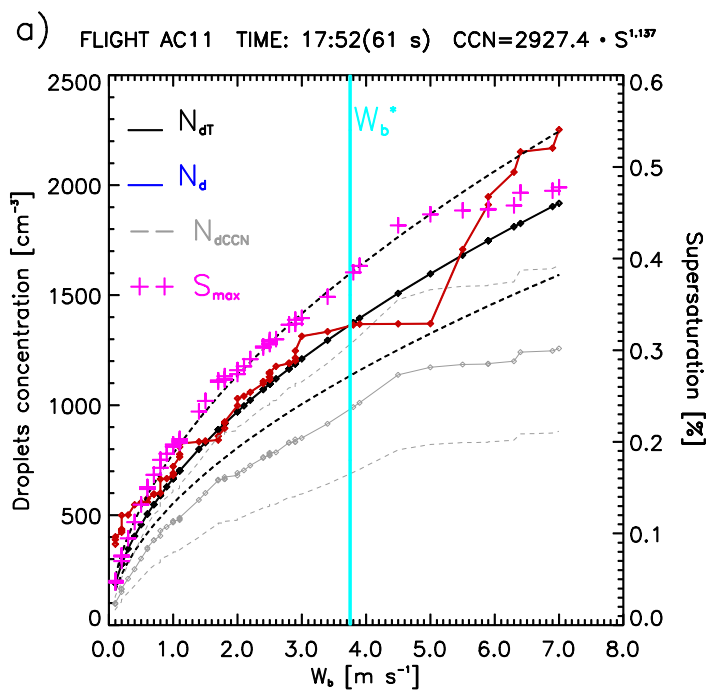
1160

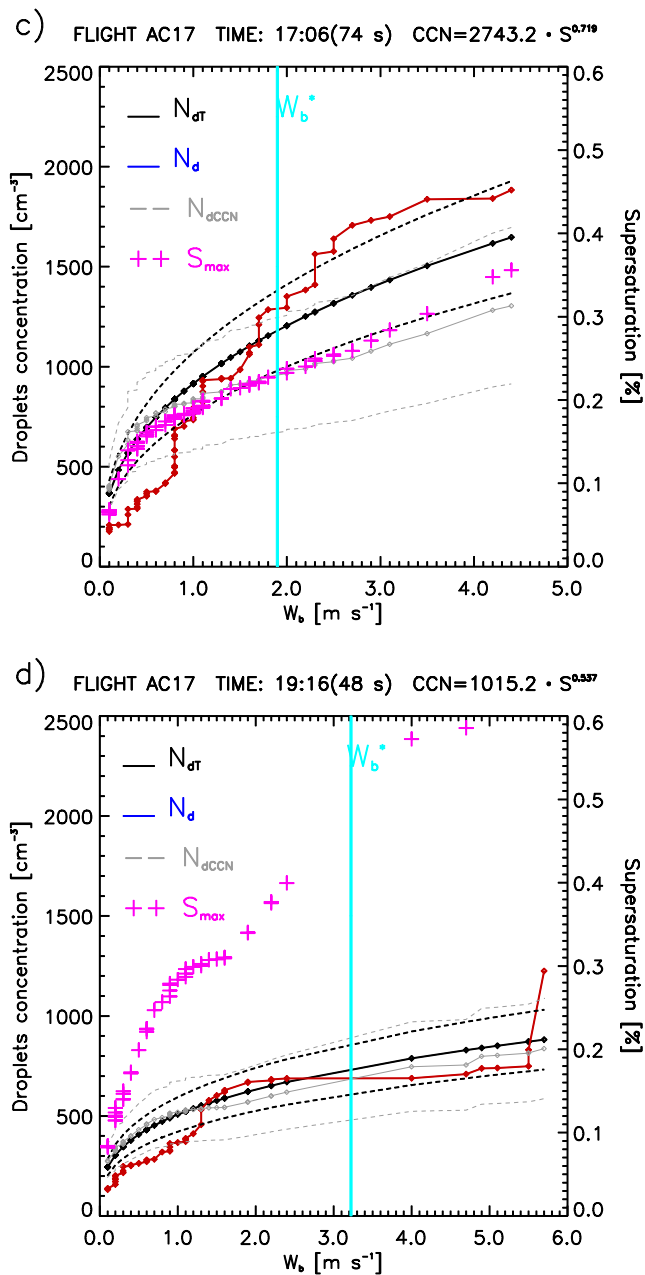






1170 Figure 11a-f. N_{dCCN} , S , N_{dAT} and N_d values are presented as a function of the cloud base updrafts (W_b). This plot is based on
 the ‘probability matching method’ (PMM), using same percentiles for W_b and N_d (N_{dCCN} or N_{dAT}). The values of N_{dCCN} , N_{dAT}
 and N_d are shown the left y-axis, those of S on the right y-axis. The black dashed lines are the N_{dAT} uncertainties. The gray
 solid (dashed) lines are the N_{dCCN} values (uncertainties). The effective updraft W_b^* for each flight segment is shown by the
 1175 cyan line. The data are based on the CAS-DPOL probe. The time, period of measurements (sample size in seconds), and
 $CCN(S)$ equation are shown on the top of the figures.

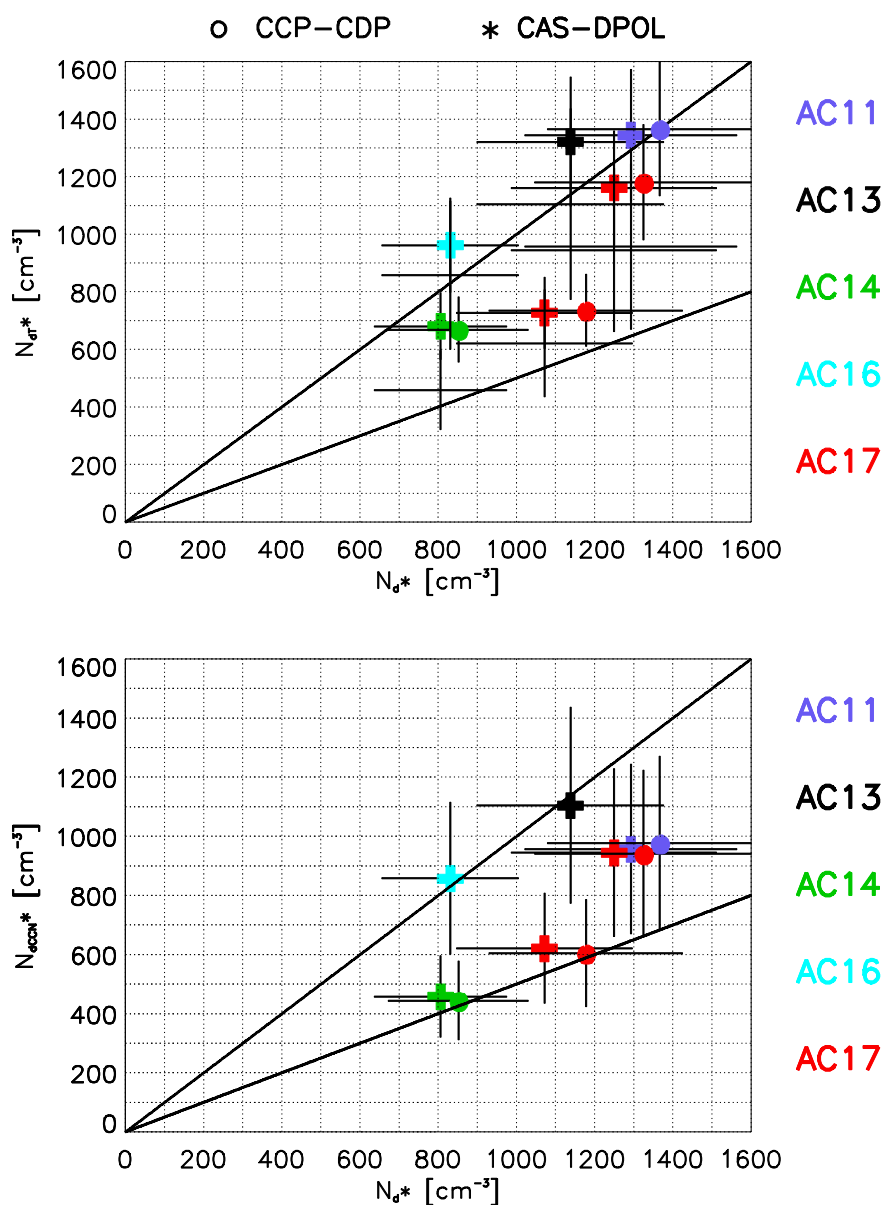




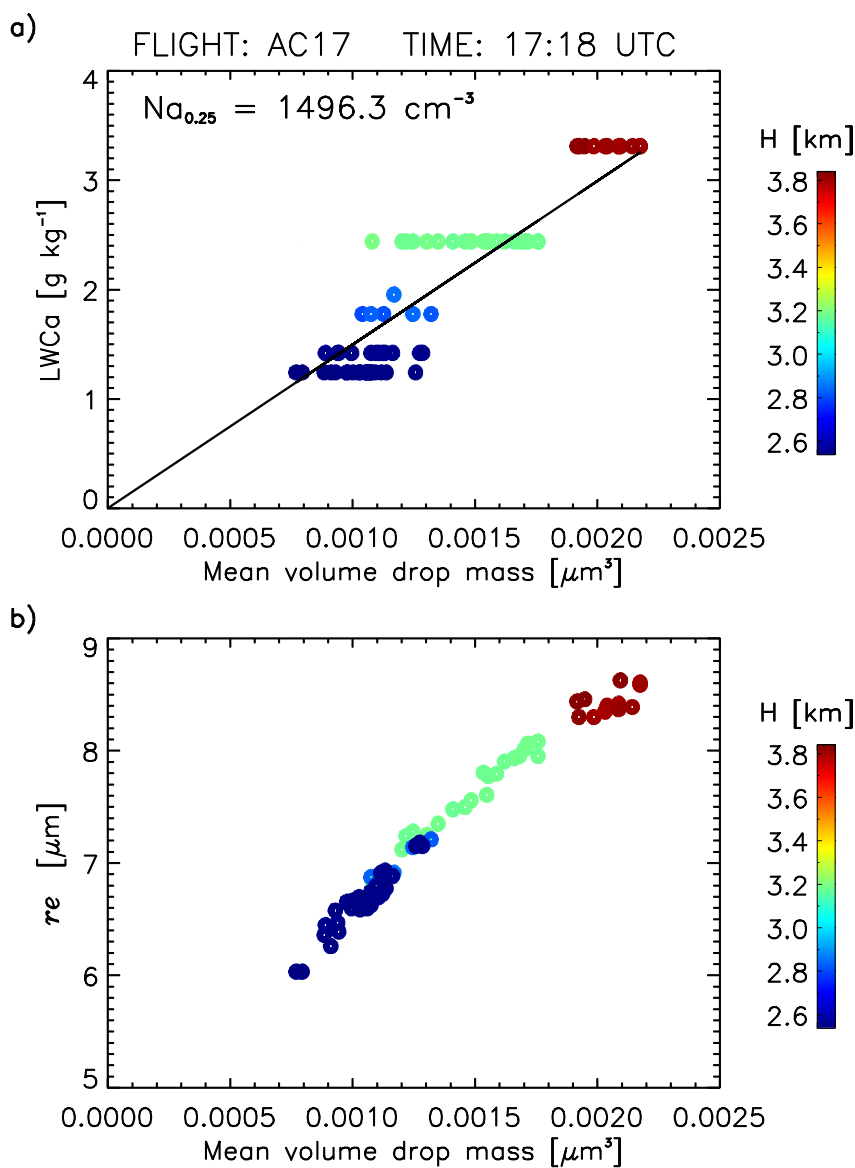
1180

1185

Figure 12a-d. Same as Figure 7 for the CCP-CDP probe. No data were available for flight AC16. The CCP-CDP malfunctioned in flight AC13 during the cloud base measurements.



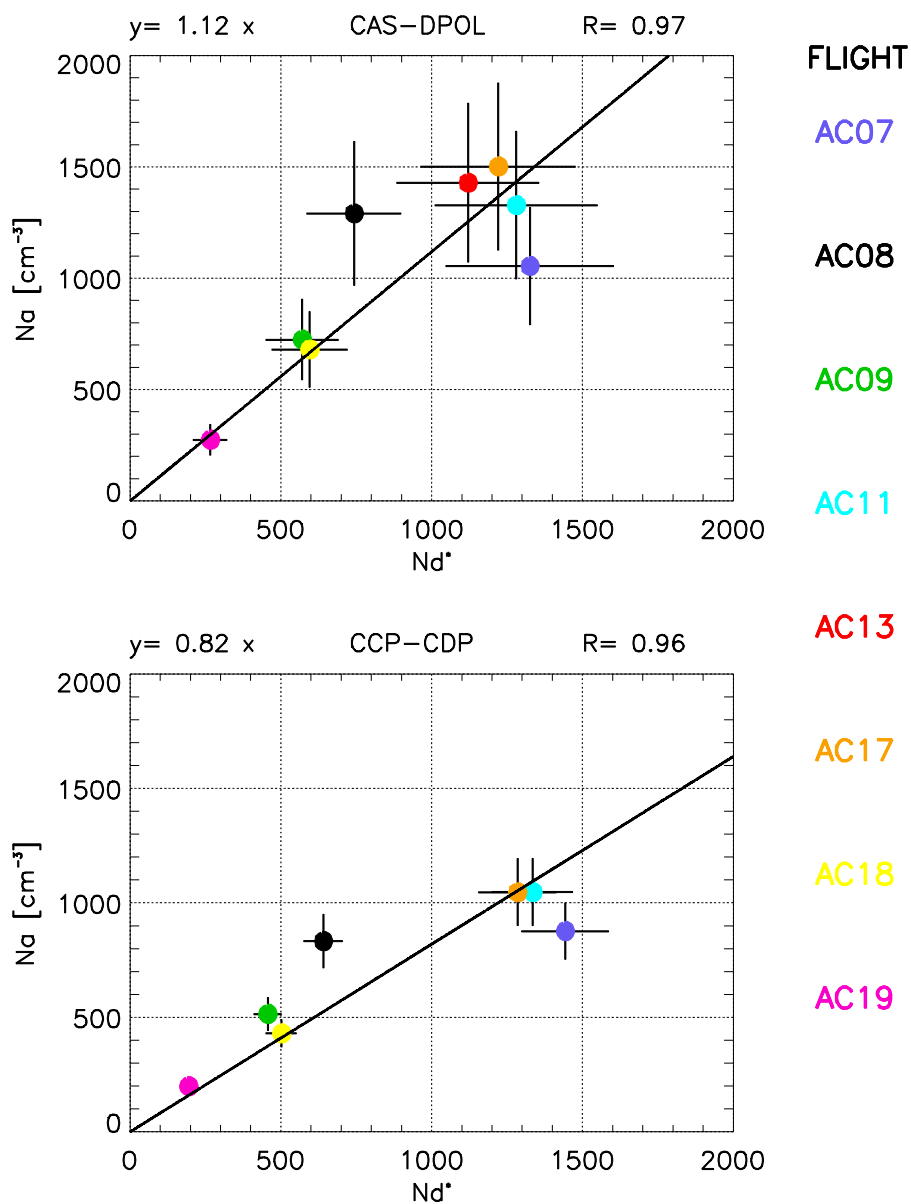
1190 Figure 13. a) N_d^* versus N_{dT}^* calculated with W_b^* from cloud base data shown in Figures 7-8. The CAS-DPOL values are indicated by plus symbols (+) and the CCP-CDP values are indicated by circles (o). The colors indicate each flight segment (legend in the right side of the plot). Error bars indicate the uncertainties of variables estimates. Lines show the 1:1 and 1:2 relationships between N_{dT}^* versus N_d^* for each probe (dotted line – CCP-CDP; solid line – CAS-DPOL); b) Same for N_d^* versus N_{dCCN}^* .



1195

1200

Figure 14 a). Mean volume drop mass (M_v) versus liquid water content from the CCP-CDP measurements for adiabatic fraction greater than 0.25 (LWC_a). Values are shown with different colors labeled as a function of height in kilometers above sea level (indicated by the colorbar on the right side of the graphic). The slope of the linear equation is the estimated N_a (i.e., 1496 cm^{-3}); b) M_v versus r_e as a function of height in kilometers above sea level (indicated by the colorbar on the right side of the graphic).



1205 Figure 15. N_a^* versus N_a measured with CAS-DPOL and CCP-CDP (indicated on the top of panels) for profile flights during the ACRIDICON-CHUVA campaign. The color of the dots is associated with the flight number shown at the right side of the panels. Error bars indicates the uncertainties of variables estimates. The linear regression equation and the correlation coefficient R are shown in the top of each panel.